

# The behaviour of the scalar gradient across the turbulent/non-turbulent interface in jets

Tiago S. Silva and Carlos B. da Silva<sup>a)</sup>

LAETA, IDMEC, Instituto Superior Técnico, Universidade de Lisboa, Lisboa, Portugal

(Received 6 February 2017; accepted 28 July 2017; published online 18 August 2017)

The dynamics of a passive scalar field near a turbulent/non-turbulent interface is analysed through direct numerical simulations of turbulent planar jets, with Reynolds numbers ranging from  $142 \leq Re_\lambda \leq 246$ , and Schmidt numbers from  $0.07 \leq Sc \leq 7.0$ . A scalar-gradient turbulent/non-turbulent interface (SG-TNTI) forms at the outer edge of the jet, which does not coincide with the vorticity turbulent/non-turbulent interface (VO-TNTI) for the lower Schmidt number cases ( $Sc = 0.07$  and  $0.7$ ). Specifically, for  $Sc = 0.07$  and  $0.7$ , the scalar gradient maxima, and thus the bulk of the mixing takes place in the irrotational region, between 10 and 30 Kolmogorov micro-scale distances from the start of the VO-TNTI. For these moderate Schmidt number cases, the SG-TNTI exhibits an *irrotational-diffusive superlayer*, where the scalar gradient diffusion dominates, while the production is negligible, followed by an *irrotational-straining sublayer* where the scalar gradient production dominates. In contrast for  $Sc = 7.0$ , the SG-TNTI consists of a *viscous-convective superlayer* that closely matches the viscous superlayer from the VO-TNTI and an *inertial-convective sublayer*, where scalar gradient production dominates, which is much smaller than the turbulent sublayer of the VO-TNTI. The scaling laws and mean thicknesses of each one of these (sub)layers are briefly discussed. This work presents a systematic study of the effects of the Schmidt number on the scalar gradient evolution and of the SG-TNTI characteristics. *Published by AIP Publishing.* [<http://dx.doi.org/10.1063/1.4997951>]

## I. INTRODUCTION

Turbulent mixing is a subject of continuous interest in fluid mechanics due to its relevance to engineering and geophysical flows.<sup>1</sup> Pollutant dispersion in the atmosphere and chemical reactions inside reactors are just two examples of important problems governed by the fine scale details of the transport of scalars and where an accurate prediction of the scalar mixing rates is absolutely crucial.

A related fundamental problem involving the transport of scalars occurs near turbulent/non-turbulent interfaces (TNTI).<sup>2</sup> These sharp and strongly inhomogeneous layers occur in most canonical free shear flows such as in jets, wakes and mixing layers, and also in boundary layers and have been studied in many recent works. The majority of these works focus on the dynamics of vorticity near the TNTI, since the important mechanism of turbulent entrainment essentially involves the “communication” of vorticity from the turbulent core region (T) of the flow into the irrotational or non-turbulent (NT) region.

In some studies turbulent entrainment has been described as large-scale eddy motions (engulfment) occurring from time to time at particular points along the TNTI (Townsend<sup>3</sup>), while recent works suggest instead that turbulent entrainment results from small scale motions (nibbling) acting along the entire TNTI (Mathew and Basu<sup>4</sup>), as described by Corrsin and Kistler.<sup>5</sup> Some flow variables, e.g., the vorticity, display a characteristic (sharp) jump at the TNTI (Westwerweel *et al.*,<sup>6,7</sup> Holzner *et al.*,<sup>8</sup> Taveira *et al.*<sup>9</sup>), and the detailed dynamics of

the vorticity and of the kinetic energy have been analysed in detail near the TNTI to understand these jumps (e.g., Holzner *et al.*,<sup>8</sup> Taveira and da Silva,<sup>10</sup> Taveira *et al.*<sup>9</sup>).

It has been shown that the TNTI has a complex two layer structure with a viscous superlayer (VSL) where the viscous enstrophy diffusion dominates and a turbulent sublayer (TSL) where the enstrophy build up is dominated by the enstrophy production,<sup>11–13</sup> where these two (sub)layers are bounded at one side by the irrotational boundary (IB)<sup>14</sup> and by the start of the turbulent core region in the other side.

Recently the dynamics of scalars near TNTI has received some attention. Westerweel *et al.*<sup>7</sup> studied the scalar transport of a passive scalar with Schmidt number  $Sc = 2000$  near the TNTI in a round jet and developed a theory to compute an eddy diffusivity near this region. Attili *et al.*<sup>15</sup> conducted the first detailed analysis of a passive scalar field (with  $Sc \approx 1$ ) near the TNTI and observed the existence of a sharp jump of this quantity near the TNTI, much sharper than for the vorticity field. Gampert *et al.*<sup>16,17</sup> studied the passive scalar thickness and the scalar dissipation near a TNTI of a jet and concluded that it scales with the Taylor micro-scale.

Probably the most thorough works dealing with the dynamics of a passive scalar near a TNTI are the ones from Watanabe *et al.*<sup>14,18,19</sup> In Watanabe *et al.*,<sup>18</sup> direct numerical simulations (DNS) of planar jets were used to study an isothermal reaction between two species supplied from the jet and ambient flow, respectively, for a Schmidt number of  $Sc = 1.0$ . They observed that the concentration of chemical species changes very quickly across the TNTI, while the width of this jump is almost independent of the Damköhler number, which was here set by modifying the reaction rate.

<sup>a)</sup>carlos.silva@tecnico.ulisboa.pt

It was moreover shown that the chemical reaction near the TNTI depends on the interface orientation, and the production rate is frequently transported by the velocity field.

Watanabe *et al.*<sup>14</sup> analysed the transport of a passive scalar near the TNTI using DNS of planar jets, where the analysis was done in relation to the enstrophy TNTI defined by a given enstrophy threshold. The analysis separated the TNTI between three different orientations and showed that both the interface propagation and molecular diffusion contribute to the scalar transport across the TNTI and that while non-turbulent fluid is frequently transported into the turbulent region across cross-streamwise and leading edges of the TNTI, turbulent fluid is often transported into the non-turbulent region across trailing edge surfaces.

Finally, Watanabe *et al.*<sup>19</sup> used DNS of mixing layers with Schmidt numbers varying between  $Sc = 0.25, 1, 4,$  and  $8$  to investigate the passive scalar transport near the TNTI, within the VSL and TSL regions. They observed that the entrainment of non-turbulent fluid operates differently within each of these two sublayers and noticed that once the fluid reaches the TSL, it tends to move in the tangential direction of the IB before being mixed within the turbulent core region. Moreover, they observed that a peak value of mean scalar dissipation appears between the TSL and VSL independently of the Schmidt number.

The characteristics and evolution of the scalar gradient near TNTIs have, however, comparatively been receiving less attention. An important exception (discussed below) is the work of Hunger *et al.*,<sup>20</sup> who analysed passive scalars with  $Sc = 1.0$  and  $Sc = 0.25$  near the TNTI in planar turbulent jets. The scalar gradient magnitude is defined as  $G^2 = G_i G_i$  where  $G_i = \partial\theta/\partial x_i$  is the scalar gradient, proportional to the loss term in the scalar ( $\theta$ ) transport governing equation, the so-called scalar dissipation rate  $\varepsilon_\theta = \gamma G_i G_i$  ( $\gamma$  is the scalar diffusivity), and  $\varepsilon_\theta$  represents the mixing rate or the rate at which scalar fluctuations are destroyed. Accurate prediction of the scalar gradient magnitude is critical in combustion applications<sup>21,22</sup> and the study of this quantity has been the object of many fundamental turbulence studies, often using homogeneous isotropic turbulence (HIT).<sup>23–25</sup> Even in HIT, it is well known that the dynamics of the scalar gradient is quite different from that of the vorticity magnitude,<sup>26,27</sup> and it is important to analyse what other differences may arise in the presence of a sharp and strongly inhomogeneous interface such as a TNTI.

In the present work, direct numerical simulations (DNS) of turbulent planar jets are used to investigate the evolution of the scalar gradient magnitude for several Schmidt numbers. Since the value of the Schmidt number strongly affects the passive scalar dynamics and in order to cover a range of different Schmidt numbers, here we assess results obtained with three different values of the Schmidt number with  $Sc < 1$ ,  $Sc \approx 1$ , and  $Sc > 1$ . Specifically, we use  $Sc = 0.07, 0.7,$  and  $7.0$ , i.e., spanning one order magnitude difference between Schmidt numbers, which permits to study different scalar dynamics, while allowing the velocity field to be typical of fully developed turbulence using present day computational capabilities. As will be shown below, a scalar-gradient turbulent/non-turbulent interface (SG-TNTI) develops in some cases, which is markedly different from the typical vorticity TNTI

(VO-TNTI). The investigation focuses on the relation between the two interfaces and establishes the different (sub)layers that occur for different Schmidt numbers. The scaling of these layers should be assessed in detail in future studies, since it may be critical for accurate predictions of the mixing processes in many engineering and environmental problems.

This article is organised as follows. Section II describes the new DNS of planar jets carried out in this study including their detailed validation. Section III introduces the main variables associated with the VO-TNTI and the SG-TNTI and describes the effects of the Schmidt number on the outer surface of the SG-TNTI. Section IV assesses the detailed dynamics of the scalar gradient for several Schmidt numbers and describes the nature and scaling of the several (sub)layers within the SG-TNTI. The work ends with an overview of the main results and a summary of the main conclusions (Sec. V).

## II. DIRECT NUMERICAL SIMULATIONS OF TURBULENT PLANAR JETS

### A. Numerical methods

The numerical simulations used in this work were carried out with a Navier-Stokes solver (incompressible flow) that uses classical pseudo-spectral methods (collocation method—Canuto *et al.*<sup>29</sup>) for spatial discretization, and a 3rd order, 3 steps Runge-Kutta scheme (Williamson<sup>30</sup>) for temporal advancement. This code is an upgraded version of the algorithm used in Ref. 31, the main difference being the decomposition of the computational domain using a 2d-pencil decomposition, which relies on the *2DECOMP&FFT* library (<http://2decomp.org>) to handle the multi core communication and three dimensional Fourier transforms. In addition to the velocity field, the simulations also include the transport of a passive scalar field. All the simulations were fully de-aliased using the 2/3 rule.

### B. Physical and computational parameters of the simulations

Three new temporal turbulent planar jet direct numerical simulations (DNS) were carried out in the present work ( $PJET_{142}^{7.0}$ ,  $PJET_{236}^{0.07}$ , and  $PJET_{246}^{0.7}$ ), whose main physical and computational details are summarised in Table I and that differ mainly in the Reynolds and Schmidt numbers. Similar planar jet simulations were used extensively by the authors and are described in detail in references, e.g., Refs. 31 and 32, and therefore only a short description is given here.

All the DNS use the same number of collocation points ( $N_x \times N_y \times N_z$ ) = (1536 × 1536 × 768) for the streamwise ( $x$ ), normal ( $y$ ), and spanwise ( $z$ ) direction, respectively, and the same computational domain, which is equal to ( $L_x \times L_y \times L_z$ ) = ( $7H \times 7H \times 3.5H$ ), where  $H$  is the inlet slot-width of the jet. The initial Reynolds and Schmidt numbers is equal to  $Re_H = (U_1 - U_2)H/\nu = 3000, 8000,$  and  $8000$  and  $Sc = \gamma/\nu = 7.0, 0.07$  and  $0.7$ , for simulations  $PJET_{142}^{7.0}$ ,  $PJET_{236}^{0.07}$ , and  $PJET_{246}^{0.7}$ , respectively, where  $\nu$  is the kinematic viscosity,  $U_1$  is the maximum initial velocity,  $U_2$  is the minimum initial velocity, and  $\gamma$  is the scalar diffusivity. Simulations  $PJET_{236}^{0.07}$  and  $PJET_{246}^{0.7}$  differ only in the random numbers used in the initial (velocity) perturbation fields. The velocity fields of these simulations

TABLE I. Summary of the three turbulent planar jet DNS ( $PJET_{142}^{7.0}$ ,  $PJET_{236}^{0.07}$ , and  $PJET_{246}^{0.7}$ ) at  $T/T_{ref} = 24$ : Initial Reynolds number,  $Re_H$ ; Schmidt number,  $Sc$ ; number of collocation points for the streamwise ( $x$ ), normal ( $y$ ), and spanwise ( $z$ ) directions, ( $N_x \times N_y \times N_z$ ); total extent of the computational domain, ( $L_x \times L_y \times L_z$ ); Reynolds number based on the Taylor micro-scale at the self-similar regime,  $Re_\lambda$ ; resolution,  $\Delta_x/\eta$ ; ratio between the initial width of the jet  $H$ ; and the Taylor, Kolmogorov, Obukhov-Corrsin, and Batchelor length scales from inside the turbulent region  $\lambda/H$ ,  $\eta/H$ ,  $\eta_{OC}/H$ , and  $\eta_B/H$ . Notice that the velocity fields from simulations  $PJET_{236}^{0.07}$  and  $PJET_{246}^{0.7}$  are statistically equivalent. They differ in their details because of small differences in the initial (velocity) perturbation fields. The reference turbulent quantities are taken at a distance of  $300\eta$  from the TNTI where these quantities are nearly constant, e.g.,  $\eta_B = \langle \eta_B(y_1/\eta = 300) \rangle_I$ , where  $\langle \rangle_I$  represents a conditional average in relation to the TNTI position as described below.

	$Re_H$	$Sc$	$(N_x \times N_y \times N_z)$	$(L_x \times L_y \times L_z)$	$Re_\lambda$	$\Delta_x/\eta$	$\lambda/H$	$\eta/H (\times 10^3)$	$\eta_{OC}/H (\times 10^3)$	$\eta_B/H (\times 10^3)$
$PJET_{142}^{7.0}$	3000	7.0	$(1536 \times 1536 \times 768)$	$(7H \times 7H \times 3.5H)$	141.9	1.1	0.331	8.1	1.87	3.0
$PJET_{236}^{0.07}$	8000	0.07	$(1536 \times 1536 \times 768)$	$(7H \times 7H \times 3.5H)$	236.3	2.3	0.197	3.9	28.8	14.8
$PJET_{246}^{0.7}$	8000	0.7	$(1536 \times 1536 \times 768)$	$(7H \times 7H \times 3.5H)$	246.2	2.3	0.201	3.9	5.1	4.7

are thus statistically equivalent but differ in the details (e.g., the exact details of the velocity fields used in the statistics/analysis). At  $T/T_{ref} = 24$ , when the turbulent self-similar, far field/regime has been attained and where the subsequent analysis is carried out, the Reynolds number based on the Taylor micro-scale ( $\lambda$ ) is equal to  $Re_\lambda = u'\lambda/\nu \approx 142$ , 236, and 246, for simulations  $PJET_{142}^{7.0}$ ,  $PJET_{236}^{0.07}$ , and  $PJET_{246}^{0.7}$ , respectively, where  $u'$  is the root-mean-square velocity (rms) at the jet centreline. The resolution for all the simulations is between  $\Delta_x/\eta \approx 1.1$ –2.3, where  $\eta = (\nu^3/\varepsilon)^{1/4}$  is the Kolmogorov micro-scale inside the turbulent core region of the jet. All the reference values for the turbulent quantities are taken at a distance of  $300\eta$  from the TNTI since these quantities are nearly constant inside the turbulent core of the jet, e.g.,  $\eta_B = \langle \eta_B(y_1/\eta = 300) \rangle_I$ , where  $\langle \rangle_I$  represents a conditional average in relation to the TNTI position as described below. The viscous dissipation is computed as  $\varepsilon = 2\nu S_{ij} S_{ij}$  ( $S_{ij} = (\partial u_i/\partial x_j + \partial u_j/\partial x_i)/2$  is the rate-of-strain tensor). The resolution of the passive scalar field at high  $Sc$  is best assessed in relation to the Batchelor micro-scale defined as  $\eta_B = (\nu\gamma^2/\varepsilon)^{1/4} = \eta/\sqrt{Sc}$ , and for  $PJET_{142}^{7.0}$  we obtain  $\Delta x/\eta_B \approx 2.9$  ( $\Delta x/\eta_B \approx 0.6$  and 1.9 for  $PJET_{236}^{0.07}$  and  $PJET_{246}^{0.7}$ , respectively). Table I shows also the Obukhov-Corrsin micro-scale defined by  $\eta_{OC} = (\gamma^3/\varepsilon)^{1/4} = \eta/Sc^{3/4}$ .

As in da Silva and Pereira<sup>31</sup> and Stanley *et al.*,<sup>33,34</sup> the initial conditions for the velocity and passive scalar fields use a hyperbolic-tangent profile,

$$U(x, y, z) = \frac{U_1 + U_2}{2} - \frac{U_1 - U_2}{2} \tan h \left[ \frac{H}{4\theta_0} \left( 1 - \frac{2|y|}{H} \right) \right], \quad (1)$$

and

$$\Theta(x, y, z) = \frac{\Theta_1 + \Theta_2}{2} - \frac{\Theta_1 - \Theta_2}{2} \tan h \left[ \frac{H}{4\theta_0} \left( 1 - \frac{2|y|}{H} \right) \right], \quad (2)$$

where  $\theta_0$  is the initial momentum thickness, with  $U_1 = \Theta_1 = 1$  and  $U_2 = \Theta_2 = 0$ , to which a three-component velocity and passive scalar fluctuating “spectral noise” was superimposed by a convolution function that restricts the initial velocity and scalar noise to the initial shear layer region of the jet. The rate between the initial momentum thickness and jet width is equal to  $H/\theta_0 = 35$  both for the velocity and passive scalar initial mean profiles, and the amplitude of spectral noise was 5% of the maximum velocity in order to accelerate the transition to the turbulent regime quickly attain a fully developed turbulent state (1% amplitude was used for

the passive scalar noise), similarly to da Silva and Pereira<sup>31</sup> and Stanley *et al.*<sup>33,34</sup>

### C. Assessment of the direct numerical simulations

As in da Silva and Pereira<sup>31</sup> extensive validation tests were undertaken and showed that the three simulations are accurate at the large and small scales and are representative of a fully developed turbulent plane jet. By  $T/T_{ref} \approx 24$ , where  $T_{ref} = H/(2U_1)$ , the self similar regime has already been attained, and the simulations were halted before the effect of the boundary conditions could be observed in the jet statistics, e.g., the Reynolds stresses.

Figure 1 shows the coherent structures for  $PJET_{246}^{0.7}$  in the form of iso-surfaces of the second invariant of the velocity

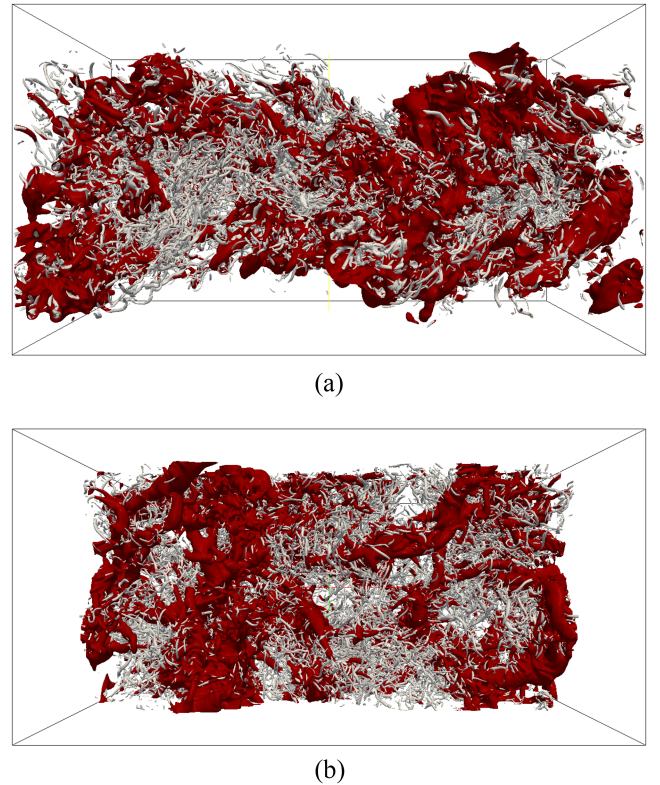


FIG. 1. Iso-surfaces of  $Q = 8(U_1/H)^2$  (grey/white) and pressure  $p = -0.08 (\rho U_1^2)$  (red/dark) for simulation  $PJET_{246}^{0.7}$  at the self-similar regime ( $T/T_{ref} \approx 24$ ). The side view shows the  $(x, y)$  planes, while the top view displays planes  $(x, z)$ . The flow is from left to right. Note that figures do not show the total extent of the computational domain along  $z$  and  $y$  ( $L_z$  and  $L_y$ ), respectively. (a) Sideview and (b) topview.

gradient tensor  $\mathcal{Q} = \frac{1}{4} (\omega_i \omega_i - 2S_{ij}S_{ij})$  and low pressure. The pressure shows highly fragmented large scale structures that are the remnants of the Kelvin-Helmoltz vortices generated during the transition period to turbulence, while  $Q > 0$  shows the more intense small scale eddies. The apparent lack of organisation and orientation of these structures is the imprint of the relatively high Reynolds number attained in the present DNS.

Figure 2 shows contours of vorticity magnitude in a  $(x, y)$  plane for  $PJET_{142}^{7.0}$ ,  $PJET_{236}^{0.07}$ , and  $PJET_{246}^{0.7}$ . As can be seen the vorticity field of  $PJET_{236}^{0.07}$  and  $PJET_{246}^{0.7}$  is not equal but very similar. The  $PJET_{142}^{7.0}$  is similar in nature but displays a smaller range of existing scales as expected due to the smaller Reynolds number; however, all three figures show a vorticity field that is typical of a fully developed turbulent regime.

Figure 3 shows contours of passive scalar in a  $(x, y)$  plane for  $PJET_{142}^{7.0}$ ,  $PJET_{236}^{0.07}$ , and  $PJET_{246}^{0.7}$  (not the same  $z$  planes as in the previous figure) clearly showing the effect of the Schmidt number on the spatial characteristics of the passive scalar in the far field of the jet. The highly diffusive nature of  $PJET_{236}^{0.07}$  ( $Sc = 0.07$ ) strongly contrasts with the sharp gradients observed in  $PJET_{142}^{7.0}$ , where the scalar advection mostly controls the scalar transport. An example of an apparent large scale engulfment event appears at the lower shear layer, in  $(x, y) \approx (0.5, -1)$  [Fig. 3(c)]. The case  $PJET_{246}^{0.7}$  is somehow between the two

other cases, displaying regions with both significant scalar diffusion and intense scalar gradients.

The DNS were compared with DNS of planar jets<sup>34–37</sup> and experiments,<sup>38–41</sup> and it was observed that the one point statistics are self-similar for  $T/T_{ref} \gtrsim 24$ . Figures 4(a)–4(c) show profiles of one point statistics at the self similar far-field region. These profiles were obtained in the following way: once the self-similar time is attained, two instantaneous (closely spaced) fields were taken. The mean profiles are obtained by averaging the flow variables for these fields along the homogeneous flow directions ( $x$  and  $z$ ), and the obtained profiles are then “folded” along the centreline/central place to improve the statistics. The degree of convergence for these profiles is not perfect but similar to what is typically found in temporal planar jet simulations<sup>31,42</sup> or temporal wakes.<sup>43</sup> The mean velocity, mean passive scalar, and streamwise Reynolds stress profiles all show reasonably good agreement with the experimental and numerical data available, and the same is true for the other Reynolds stress components (not shown). The small differences observed for the velocity field statistics in  $PJET_{236}^{0.07}$  and  $PJET_{246}^{0.7}$  are due to the differences in the initial perturbation fields and insufficient samples/fields.

Figure 5 shows the probability density functions (PDFs) of the passive scalar concentration at several points for different

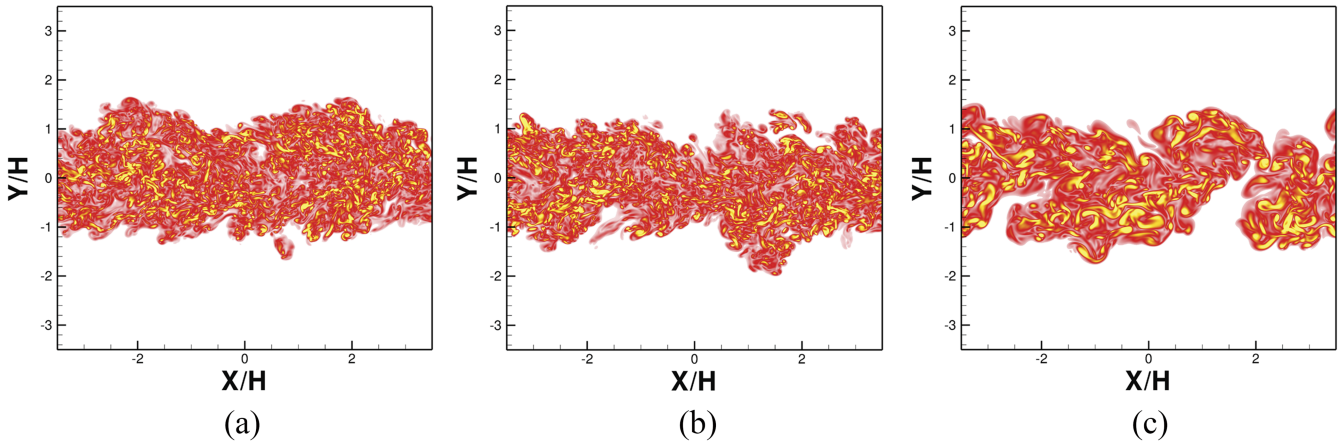


FIG. 2. Contours of vorticity magnitude in a  $(x, y)$  plane for all the DNS used in the present work at  $T/T_{ref} = 24$ . (a)  $PJET_{236}^{0.07}$ , (b)  $PJET_{246}^{0.7}$ , and (c)  $PJET_{142}^{7.0}$ .

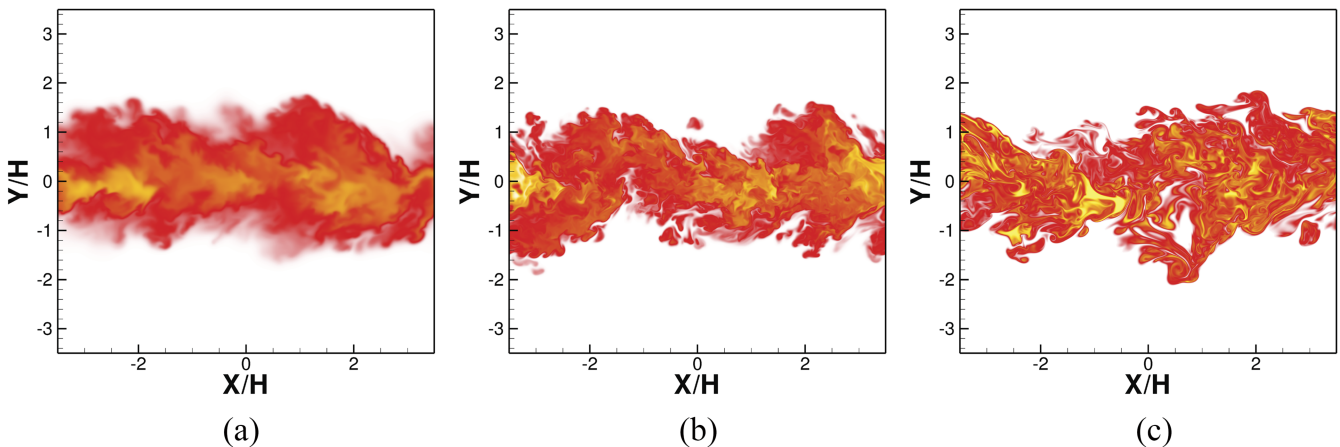


FIG. 3. Contours of passive scalar in an  $(x, y)$  plane for all the DNS used in the present work, at  $T/T_{ref} = 24$ . (a)  $PJET_{236}^{0.07}$ , (b)  $PJET_{246}^{0.7}$ , and (c)  $PJET_{142}^{7.0}$ .

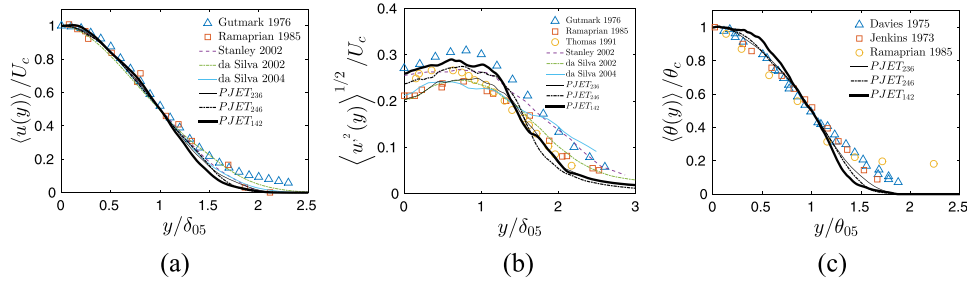


FIG. 4. Profiles of several one point statistics at the self-similar region for the three simulations,  $PJET_{236}^{0.07}$ ,  $PJET_{246}^{0.7}$ , and  $PJET_{142}^{7.0}$  compared with experimental and DNS results from Gutmark and Wynansky,<sup>38</sup> Ramaprian and Chandrasekhara,<sup>39</sup> Jenkins and Goldschmidt,<sup>41</sup> Davies *et al.*,<sup>40</sup> Stanley *et al.*,<sup>34</sup> da Silva and Métais,<sup>35</sup> and da Silva and Pereira.<sup>36</sup>  $U_c$  and  $\theta_c$  are the mean streamwise velocity and mean passive scalar concentration, respectively, at the jet centerline, and  $\delta_{0.5}$  and  $\theta_{0.5}$  are the half-widths for the velocity and passive scalar profiles, respectively. (a) Mean streamwise velocity, (b) Streamwise Reynolds stresses, and (c) Mean passive scalar.

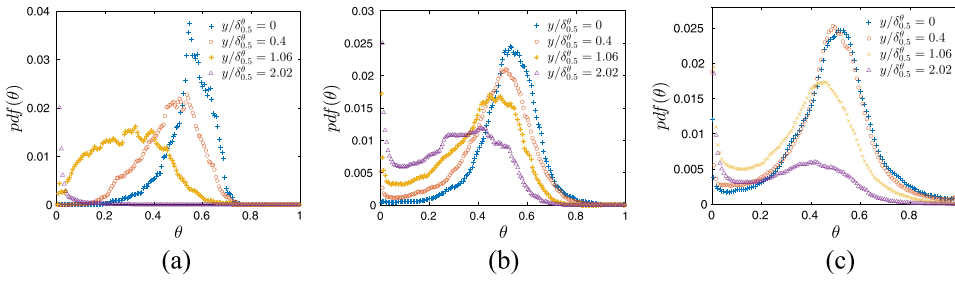


FIG. 5. Probability density functions of passive scalar concentration at several positions for different cross-wise positions ( $y$ ) for all the DNS carried out in this work, at  $T/T_{ref} = 24$ . (a)  $PJET_{236}^{0.07}$ , (b)  $PJET_{246}^{0.7}$ , and (c)  $PJET_{142}^{7.0}$ .

cross-wise positions ( $y$ ) for all the DNS. In the irrotational region ( $y/\delta_{0.5} = 2$ ), the PDFs peak at  $\theta = 0$  (zero concentration), but as one moves into the jet centreline ( $y/\delta_{0.5} \rightarrow 0$ ), the peaks of the PDFs progressively move into higher values of the concentration near  $\theta \approx 0.6$  (which is equal to  $\approx \langle \theta(y=0) \rangle$  at this instant). The shape of these PDFs is similar to those observed in several previous works (e.g., Rogers and Moser<sup>43</sup>) and indicates that by  $T/T_{ref} = 24$  the passive scalar in the present simulations has already gone through the well known “mixing transition” described in Dimotakis.<sup>1</sup>

Finally, Figs. 6(a)–6(f) show 2D (bi-dimensional) spectra for the velocity and passive scalar fluctuations at the jet central plane ( $y = 0$ ) for all the DNS. The high Reynolds number attained is shown in the similarity between the several

velocity components  $E_u(k\eta)/(\epsilon^{2/3}\eta^{5/3})$ ,  $E_w(k\eta)/(\epsilon^{2/3}\eta^{5/3})$ ,  $E_v(k\eta)/(\epsilon^{2/3}\eta^{5/3})$ , as well as the existence of the typical  $-5/3$  inertial sub-range region, which has a smaller extent for  $PJET_{142}^{7.0}$  than for the other simulations. The smooth decay observed at high Reynolds numbers demonstrates that the small scales are well resolved. The passive scalar spectra display similar characteristics, although the  $-17/3$  and  $-1$  ranges predicted for very low and very high Schmidt numbers, respectively,<sup>44</sup> are difficult to observe in the present DNS. The analysis of the three DNS clearly shows that both the velocity and scalar fields are well resolved and are representative of fully developed velocity and scalar fields in a turbulent jet. The comparison of the cases with  $Sc = 0.07$  and  $Sc = 0.7$  is straightforward because they have statistically equal velocity

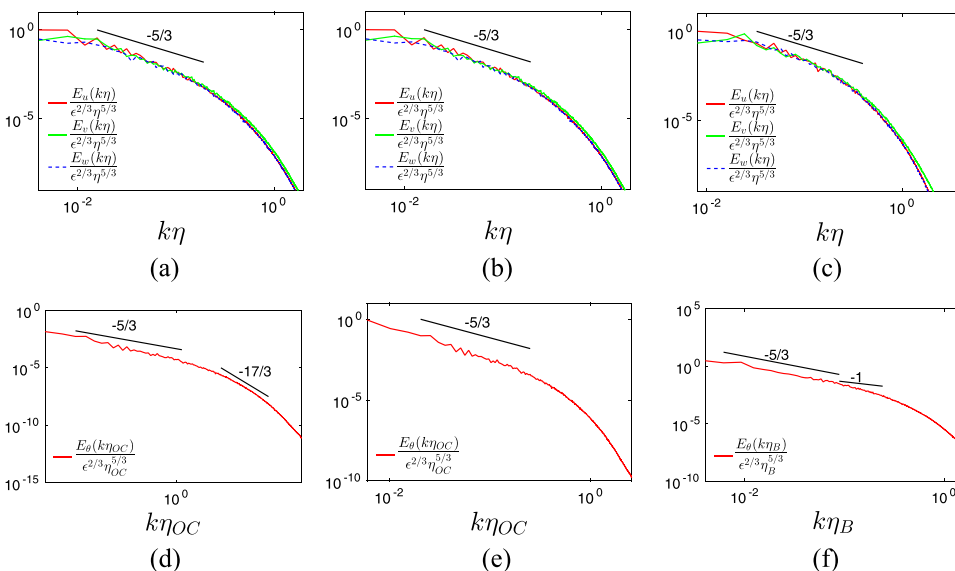


FIG. 6. 2D (bi-dimensional) spectrum of the velocity and passive scalar fluctuations taken from the jet centreline plane ( $y = 0$ ) for the several DNS. (a)  $PJET_{236}^{0.07}$ , (b)  $PJET_{246}^{0.7}$ , (c)  $PJET_{142}^{7.0}$ , (d)  $PJET_{236}^{0.07}$ , (e)  $PJET_{246}^{0.7}$ , and (f)  $PJET_{142}^{7.0}$ .

fields and differ only on the Schmidt number, while the case with  $Sc = 7.0$ , even if it has a smaller Reynolds number, is still clearly above  $Re_\lambda > 100$  needed to observe the dissipation law. Thus the three cases are statistically similar, which allows us to study the three different Schmidt number cases.

### III. THE TURBULENT/NON-TURBULENT INTERFACE OF THE VORTICITY AND SCALAR GRADIENT

When analysing the TNTI for the velocity and scalar fields generally two interfaces need to be considered. Due to the different mechanisms governing the velocity (and enstrophy) and the passive scalar (and scalar gradient), even if, as in the present work, the two interfaces initially coincide, they will eventually separate and their ultimate location will differ. One has to speak, therefore, of a vorticity turbulent/non-turbulent interface (VO-TNTI) and of a scalar gradient turbulent/non-turbulent interface (SG-TNTI). Section III A revises the VO-TNTI that prepares the discussion of the SG-TNTI, which is the main focus of the present work.

#### A. The velocity/vorticity turbulent/non-turbulent interface (VO-TNTI)

The study of the velocity/vorticity turbulent/non-turbulent interface (VO-TNTI) starts by defining the irrotational boundary (IB) defined in Watanabe *et al.*,<sup>14,19</sup> which marks the location of the outer edge of the TNTI. As described in Refs. 2, 9 and 19, the IB is the surface where the vorticity magnitude is equal to a certain threshold  $\omega = \omega_{th}$ , where the threshold is obtained by quantifying the volume of the turbulent region  $Vol_T$  as a function of  $\omega_{th}$ . Specifically,  $Vol_T$  decreases with increasing  $\omega_{th}$ , and there is a range of values of  $\omega_{th}$ , spanning more than one order of magnitude, where  $Vol_T$  remains approximately constant or decreases very slowly, reflecting the sharpness of the TNTI. Any value of  $\omega_{th}$  taken from this range establishes the IB position, since its location remains virtually unchanged when  $\omega_{th}$  varies. In the present work, we obtained  $\omega_{th}(H/U_1) = 0.46, 0.72$  and  $0.70$  for  $PJET_{246}^{7.0}$ ,  $PJET_{236}^{0.07}$ , and  $PJET_{246}^{0.7}$ , respectively. Notice that this “volume method” is mathematically equal to the “minimum PDF method” described in Prasad and Sreenivasan<sup>45</sup> as has been recently shown by da Silva *et al.*<sup>46</sup>

Conditional statistics with respect to the distance from the TNTI have been an important tool in the study of the flow near the TNTI and have been used in many research references, e.g., Refs. 2, 6, 31 and 47; therefore, only a short description is given here. Figure 7 shows the IB (dashed line) detected with vorticity criteria described above in a  $(x, y)$  plane of  $PJET_{246}^{0.7}$ . The figure shows also the global jet axis  $(x, y)$  and a zoom of the TNTI layer indicating several of the sublayers described in the subsequent text: the viscous superlayer (VSL),<sup>12</sup> turbulent sublayer (TSL),<sup>2</sup> and the TNTI layer<sup>11</sup> (encompassing the two sub-layers), with thicknesses  $\delta_v$ ,  $\delta_\sigma$ , and  $\delta_\omega$ , respectively.

Once the IB has been determined a local 2D axis ( $y_l$ ) is placed at its origin and pointing towards the T region, both at the upper and lower shear layers, as represented in Fig. 7. Conditional statistics are then computed as a function of the distance  $y_l$  from the TNTI layer using this (2D) local normal to the IB surface (only slight differences are observed when using

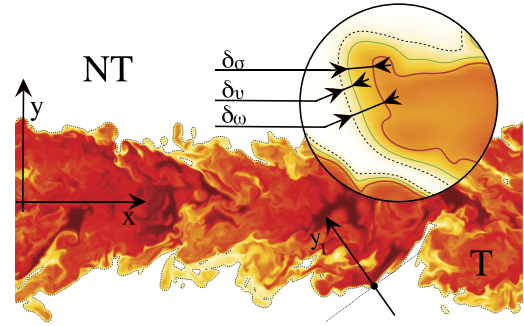


FIG. 7. Sketch of the TNTI layer separating the turbulent (T) from the irrotational or non-turbulent (NT) regions, where darker/lighter colours represent more/less intense values of scalar concentration for simulation  $PJET_{246}^{0.7}$ . The coordinate system of the plane jet  $(x, y)$  and the one used in the conditional statistics in relation to the distance from the TNTI ( $y_l$ ) are also shown. The irrotational boundary<sup>14,19</sup> defined by the selected vorticity threshold ( $\omega_{th}$ ) is denoted by a dashed line, while the viscous superlayer (VSL),<sup>12</sup> turbulent superlayer (TSL),<sup>2</sup> and the TNTI layer<sup>11</sup> (encompassing the two sub-layers), with thicknesses  $\delta_v$ ,  $\delta_\sigma$ , and  $\delta_\omega$ , respectively, are also represented where the middle (green) line represents the end of the VSL/start of the TSL and the inner (red) line represents the end of the TSL/start of the T (core) region.

a 3D local normal). Occasionally the local axis  $y_l$  intersects bubbles of irrotational flow inside the turbulent region, as well as islands of turbulent flow in the irrotational region, but these events are discarded from the statistical sample. In the present work these conditional statistics are denoted by  $\langle \rangle_l$ .

Figure 8 shows typical conditional mean profiles of  $|\omega_z|$ , where  $\omega_z$  is the spanwise vorticity component, and  $\omega_i = \varepsilon_{ijk} \partial u_j / \partial x_k$  is the curl of the velocity field  $u_i$ , for all the simulations used in the present work. The IB is by definition located at  $y_l = 0$ , while the irrotational (NT) and turbulent (T) regions are defined by  $y_l < 0$  and  $y_l > 0$ , respectively. The distance  $y_l$  is normalised by the Kolmogorov micro-scale  $\eta$  and by the Taylor micro-scale  $\lambda$ , both computed inside the turbulent region where their values are approximately constant, i.e.,  $\eta = \eta(y_l \gg 0)$ . The vorticity component  $\omega_z$  has a sharp jump at the TNTI and becomes almost constant inside the turbulent zone, and for the smaller Reynolds number case  $\langle |\omega_z| \rangle_l$  displays a characteristic bump at the start of the turbulent region in agreement with Refs. 7, 47, and 11. The intense vorticity structures tend to be tangent to the TNTI,<sup>48</sup> and this explains the particular shape of  $\omega_z$ . The fact that this feature is less clear for the higher Reynolds number cases is possibly caused by the more

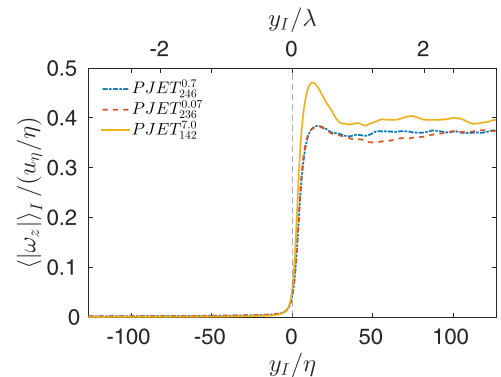


FIG. 8. Mean conditional profiles of  $\langle |\omega_z| \rangle_l$  normalized by the Kolmogorov length and velocity scales for all the DNS carried out in the present work. The upper axis with the Taylor scale normalisation corresponds to  $PJET_{246}^{0.7}$  only.

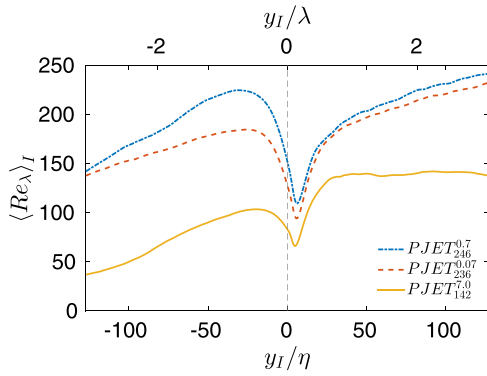


FIG. 9. Mean conditional profiles of Reynolds number based on the Taylor micro-scale  $\langle Re_\lambda \rangle_I$  for all the DNS carried out in the present work. The upper axis with the Taylor scale normalisation corresponds to  $PJET_{246}^{0.7}$  only.

fragmented and less “coherent” shape of the intense vortices at higher Reynolds numbers.

Figure 9 shows conditional profiles of the Taylor based Reynolds number defined as

$$\langle Re_\lambda \rangle_I = \left( \frac{5}{3\nu \langle \epsilon \rangle_I} \right)^{1/2} \langle u'_i u'_i \rangle_I, \quad (3)$$

where  $\langle u_i'^2 \rangle_I$  is computed by<sup>6,10,47</sup>

$$\langle u_i'^2 \rangle_I = \langle u_i^2 \rangle_I - \langle u_i \rangle_I^2. \quad (4)$$

After a sharp rise in the beginning of the turbulent region,  $Re_\lambda$  attains a constant value or rises more slowly, indicating that the Reynolds number is consistently high for the majority of the flow region neighbouring the TNTI for all the DNS used in this work. The particular reference values of  $Re_\lambda$  defining each simulation are taken at  $y_I/\eta \approx 300$ , which is near the jet centreline and thus representative of the turbulent core region.

In order to define the several sublayers existing inside the TNTI layer, it is important to review the enstrophy and the scalar gradient transport equations; however, these equations need to be analysed in a local coordinate system fixed at the moving IB, and it is therefore necessary to take into account the TNTI propagation velocity (Holzner and Lüthi,<sup>49</sup> Watanabe *et al.*<sup>19</sup>).

The velocity of the interface  $\mathbf{U}_I$  can be decomposed into two components,<sup>19,49</sup> the fluid velocity at the interface,  $\mathbf{U}(x_0)$ , where  $x_0$  is the interface position in a fixed coordinate system

and the TNTI propagation velocity  $\mathbf{V}_P$ , which is the velocity of the interface iso-surface relative to fluid velocity, i.e.,

$$\mathbf{U}_I = \mathbf{U}(x_0) + \mathbf{V}_P. \quad (5)$$

The Lagrangian material time derivative of any random function  $f$  at a point in  $x = x_I + x_0$  in relation to the local coordinate system  $x_I$  is

$$\frac{Df}{Dt} = \frac{\partial f}{\partial t} + (\mathbf{U}(x_I + x_0) - \mathbf{U}_I) \cdot \nabla f. \quad (6)$$

The enstrophy  $\omega^2/2$  ( $=\omega_i\omega_i/2$ ) transport equation in the local coordinate frame becomes<sup>19</sup>

$$\underbrace{\frac{\partial \omega^2/2}{\partial t}}_{\text{Temp. Variation}} = - \underbrace{(\mathbf{U}(x_I + x_0) - \mathbf{U}(x_0) - \mathbf{V}_P^\omega)}_{\text{Convection}} \cdot (\nabla \omega^2/2) + \underbrace{\omega_i \omega_j S_{ij}}_{\text{Production}} + \underbrace{\nu \nabla^2 (\omega^2/2)}_{\text{Diffusion}} - \underbrace{\nu (\nabla \omega)^2}_{\text{Dissipation}}, \quad (7)$$

where  $\mathbf{V}_P^\omega$  is the propagation velocity of the vorticity interface and the right-hand side terms of the equation represent the convective, production, viscous diffusion, and viscous dissipation terms, respectively. Since the IB is by definition an iso-surface defined by a constant vorticity magnitude threshold,  $\omega_{th}$ , the material time derivative is zero at the interface position, i.e.,  $\partial(\omega^2/2)/\partial t' = 0$ , and thus the vorticity propagation velocity can be computed using Eq. (7), yielding

$$\mathbf{V}_P^\omega = - \left( \frac{2\omega_i \omega_j S_{ij}}{|\nabla \omega^2|} + \frac{2\nu \nabla^2 (\omega^2/2)}{|\nabla \omega^2|} - \frac{2\nu (\nabla \omega)^2}{|\nabla \omega^2|} \right) \frac{\nabla \omega^2}{|\nabla \omega^2|}, \quad (8)$$

where the first and second and third terms in the right-hand side of Eq. (8) represent the inviscid and viscous contributions to  $\mathbf{V}_P^\omega$ , respectively.<sup>42</sup>

Figure 10 shows the conditional enstrophy budget [Eq. (7)] for the simulation  $PJET_{236}^{0.07}$ , with the identification of each one of the TNTI sublayers, mentioned in relation to Fig. 7. Except near the TNTI ( $y_I \approx 0$ ), the enstrophy dynamics is dominated by the production  $\omega_i \omega_j S_{ij}$  and dissipation  $-\nu (\partial \omega_i / \partial x_j)^2$ , and all the other terms are negligible (the small oscillations in the advection and temporal variation is due to insufficient samples).

Moving from the irrotational ( $y_I \ll 0$ ) into the turbulent region ( $y_I \gg 0$ ), the initial growth of enstrophy across the TNTI (in  $0 \lesssim y_I/\eta \lesssim 4$ ) is prompted by the viscous diffusion

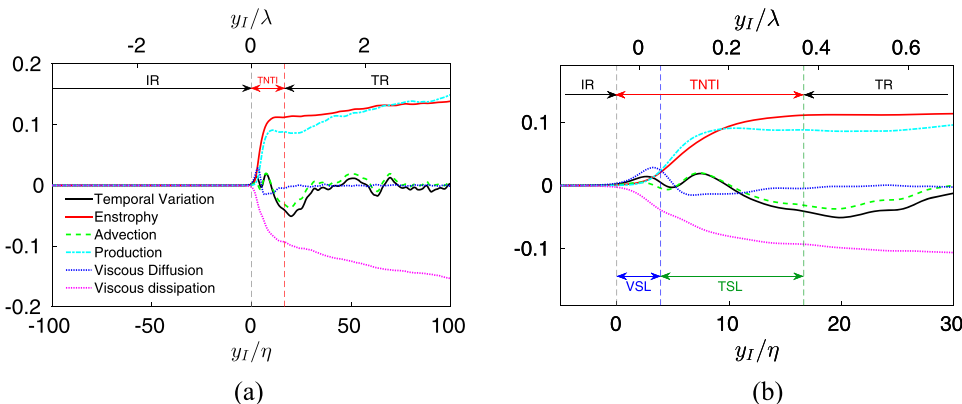


FIG. 10. Conditional enstrophy and enstrophy budget [represented by the terms from Eq. (7)] for simulation  $PJET_{236}^{0.07}$ , as a function of the distance to the TNTI  $y_I$ , normalised by the Kolmogorov  $\eta$ , and by the Taylor micro-scale  $\lambda$ , from (a)  $-100 \leq y_I/\eta \leq +100$  and (b)  $-5 \leq y_I/\eta \leq 30$ . The viscous superlayer (VSL) and turbulent sublayer (TSL) within the TNTI (previously depicted in Fig. 7) are also shown.

$v\partial^2/\partial x_j\partial x_j(\omega_i\omega_i/2)$ , while later ( $4 \lesssim y_l/\eta \lesssim 17$ ) the production dominates, and the viscous diffusion becomes negligible. When the enstrophy ceases to grow and attains an approximate plateau, we have reached the turbulent core region ( $y_l/\eta \gtrsim 17$ ). Similar conditional enstrophy budgets have been observed in TNTIs from very different flow types.<sup>7,8,12,19,47,50</sup>

The TNTI [Fig. 10(b)] is delimited by the irrotational region (IR) and by the turbulent core region (TR) and contains two adjacent sublayers defined by the relative importance between the enstrophy production and viscous diffusion: the viscous superlayer (VSL), with mean thickness  $\langle\delta_v\rangle$  is the sublayer within the TNTI where viscous diffusion dominates, and the turbulent sublayer (TSL), with mean thickness  $\langle\delta_\sigma\rangle$ , where enstrophy production outweighs viscous diffusion. The location of the boundaries delimiting these layers was computed as follows: the IB was obtained as the surface where  $\partial^2 Vol_T(\omega_{ir})/\partial\omega_{ir}^2 = 0$ , where  $Vol_T(\omega_{ir})$  is the volume of the flow where the local vorticity magnitude is above the threshold  $\omega_{ir}$  (Watanabe *et al.*<sup>19</sup>). The end of the VSL is defined by the point where the enstrophy production becomes bigger than the enstrophy diffusion  $\omega_i\omega_j S_{ij} > v\partial^2/\partial x_j\partial x_j(\omega_i\omega_i/2)$ . Finally, the end of the TSL is defined as the location where the enstrophy attains its first local maximum. Previous works on the TNTI defined the mean TNTI thickness  $\langle\delta_\omega\rangle$  as the thickness associated with the enstrophy jump across the TNTI layer, e.g., Refs. 7, 11, and 47. The several sublayers are also depicted in Fig. 7.

## B. The scalar/scalar gradient turbulent/non-turbulent interface (SG-TNTI)

Having revised the main features of the velocity/vorticity TNTI (VO-TNTI), we now move into the analysis of the scalar/scalar gradient TNTI (SG-TNTI). The differences and similarities between the VO-TNTI and SG-TNTI have been previously analysed by Gampert *et al.*,<sup>28</sup> Watanabe *et al.*,<sup>19</sup> and Hunger *et al.*<sup>20</sup> It has been observed that while for  $Sc = 1.0$  these interfaces are almost equal,<sup>28</sup> they tend to separate for  $Sc < 1$ .<sup>20</sup> In the present work in order to detect the SG-TNTI, we have used the same technique developed for the vorticity interface, based on the turbulent volume, but using the magnitude of the scalar gradient instead,  $|G_i| = (G_i G_i)^{1/2}$ , where  $G_i = \partial\theta/\partial x_i$  is the scalar gradient vector. Figure 11 shows the turbulent volume  $Vol_T$  defined as the number of flow points where  $|G_i|$  is above a given threshold  $G_{th}$  for  $PJET_{236}^{0.07}$ . Similar figures were obtained for the other two DNS. The figure resembles the equivalent plots for the vorticity magnitude.<sup>9,46,51</sup> Again, there is a range of values of  $G_{th}$  for which  $Vol_T$  changes very slowly, which reflects the ‘‘sharpness’’ of the SG-TNTI. In the present case this range extends to  $2.1 \times 10^{-5} < G_{th} < 0.12$  and a threshold of  $G_{th} = 0.105$  was chosen. We have computed the ratio between the detection threshold and the turbulent

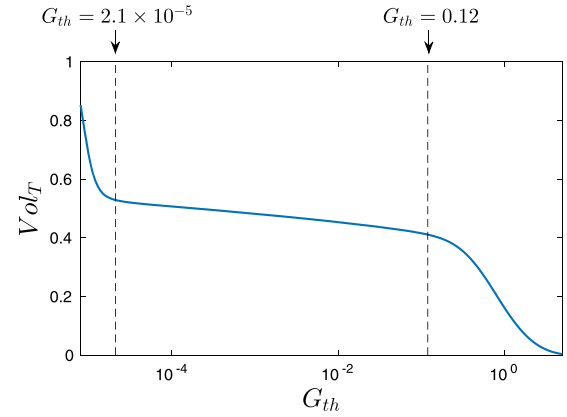


FIG. 11. Volume fraction of  $|G_i| > G_{th}$  as function of  $G_{th}$  showing the lowest and highest possible threshold values for  $PJET_{236}^{0.07}$ . In the present case a threshold of  $G_{th} = 0.105$  was chosen but any other values between the two limits has no effect on the conditional statistics.

value of the scalar gradient in the several cases and we obtained  $G_{th}/G_T = 0.05980$  for  $PJET_{236}^{0.07}$ ,  $G_{th}/G_T = 0.0347$  for  $PJET_{246}^{0.7}$ , and  $G_{th}/G_T = 0.031889$  for  $PJET_{142}^{7.0}$ . It is important to recall that, similarly as with the VO-TNTI, any other value chosen between the two limits in the plateau of  $Vol_T$  has virtually no impact on the SG-TNTI physical location and consequently on the conditional statistics.

Notice that the presently defined SG-TNTI is different from the scalar interface defined in Watanabe *et al.*,<sup>19</sup> who were more concerned with the evolution of the scalar field itself  $\theta$  and who define the scalar interface as the location of maximum magnitude of the scalar gradient  $|G_i|$ . However, with this definition passive scalar already exists after the interface is attained, and in the present work we are more interested in investigating the scalar mixing, which is proportional to  $|G_i|$ , as described in the introduction.

Figure 12 shows the scalar gradient iso-surfaces for the three DNS detected with the method described above. At first sight they resemble the vorticity TNTI (VO-TNTI) already described in many studies,<sup>10,51,52</sup> with a large number of convex shaped structures towards the irrotational region. The figure is interesting because it already points to the different nature of the SG-TNTI and its connection to the VO-TNTI underneath. The three TNTIs are clearly different, as noticed by the size and number of convolutions observed in the three interfaces. The  $PJET_{236}^{0.07}$  and  $PJET_{246}^{0.7}$  cases have almost the same Reynolds number; therefore, the observed differences only reflect modifications in the passive scalar dynamics as the Schmidt number changes. Whereas the SG-TNTI for  $PJET_{236}^{0.07}$  is relatively smooth and displays only large scale features, the SG-TNTI for  $PJET_{246}^{0.7}$  displays both small and large scale structures, and it is evident that smaller scales for the passive scalar field are present in  $PJET_{246}^{0.7}$  compared with  $PJET_{236}^{0.07}$ .

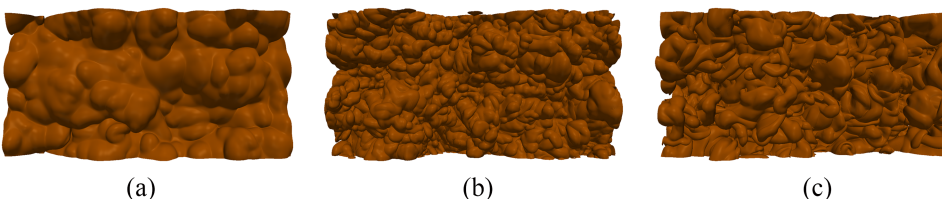


FIG. 12. Iso-surfaces of scalar gradient magnitude  $G^2$  for the upper shear layer interface detected for (a)  $PJET_{236}^{0.07}$ , (b)  $PJET_{246}^{0.7}$ , and (c)  $PJET_{142}^{7.0}$ , where the threshold for the three iso-surfaces is  $G^2 H^2 = 0.1165, 0.2321, \text{ and } 0.4951$ , respectively.

The iso-surface for  $PJET_{142}^{7.0}$  is somehow between the other two in terms of roughness. The Schmidt number is one order of magnitude higher than in  $PJET_{246}^{0.7}$ ; however, the smaller Reynolds number compensates this fact and explains why the iso-surface for  $PJET_{142}^{7.0}$  has a roughness somehow between  $PJET_{236}^{0.07}$  and  $PJET_{246}^{0.7}$ .

Figure 13 shows conditional mean profiles of passive scalar  $\theta$  and scalar gradient magnitude  $G^2 = G_i G_i$  for the three DNS and complements the previous observations. Notice that the distance from the SG-TNTI is denoted by  $y_I^\theta$  to differentiate it from the distance from the VO-TNTI, defined by  $y_I$ .

Figure 13(a) shows that sharp scalar jumps are observed for  $PJET_{142}^{7.0}$  and  $PJET_{246}^{0.7}$  and less so for  $PJET_{236}^{0.07}$ . The thickness of the scalar jump is clearly much smaller for the highest Schmidt number than for the other cases, i.e., as expected, the scalar gradient thickness decreases as the Schmidt number increases, in agreement with Watanabe *et al.*<sup>19</sup> This is also observed in the scalar gradient profiles [Fig. 13(b)], even if the magnitude of the peak is less clear because all the profiles are normalised by the turbulent values  $G_T^2$  to ease the comparison. Comparing the scalar gradient profiles with the vorticity  $|\omega_z|$  profiles described before (Fig. 8), it is obvious that the two quantities are very different with the  $\langle G_i G_i \rangle_I$  presenting a very marked peak at the SG-TNTI in agreement with previous works,<sup>14,15,19</sup> before quickly attaining a roughly constant value.

Figure 14 shows a small section of the detected velocity/vorticity TNTI (VO-TNTI) and the scalar/scalar gradient TNTI (SG-TNTI) in an  $(x, y)$  plane for the three DNS clearly showing the differences between the two layers. Generally the two interfaces do not coincide and can actually be quite far away from each other. Since at the start of all the simulations, the VO-TNTI and SG-TNTI exactly coincide, and the observed

differences result from the different interplays between the turbulent and passive scalar in the three cases. The case  $PJET_{142}^{7.0}$  is an exception to this as the high Schmidt number of this case implies that the passive scalar mixing is largely commanded by the turbulent motions caused by the VO-TNTI. Also, the distance between the VO-TNTI and SG-TNTI is much higher for  $PJET_{236}^{0.07}$  than for  $PJET_{246}^{0.7}$ , which can be explained by the very strong diffusive nature of the smaller Schmidt number case since the turbulence levels are similar in both cases. An interesting observation concerns the different levels of “roughness” that can be observed for the VO-TNTI and SG-TNTI in the same case. Consider, for example, the case  $PJET_{236}^{0.07}$ . For this simulation, the SG-TNTI is further away from the turbulent core than the VO-TNTI, as expected since  $Sc < 1$ . However, the SG-TNTI is very smooth while the VO-TNTI underneath shows a much more rough surface. This difference is less pronounced for the case  $PJET_{246}^{0.7}$  since  $Sc \approx 1$  (notice that the SG-TNTI is again outside the VO-TNTI because  $Sc < 1$ ). These results agree with the results from Gampert *et al.*<sup>28</sup> who have shown that for  $Sc = 1.0$ , the scalar and vorticity interfaces are virtually equivalent and also with the results from Hunger *et al.*<sup>20</sup> who studied for the first time the effect of the Schmidt number on the differences between the scalar and vorticity interfaces and who observed that for  $Sc < 1$ , the scalar interface does not coincide with the vorticity interface.

The different locations for the VO-TNTI and SG-TNTI in practice mean that in some instances the passive scalar mixing is somehow “detached” from the turbulent dynamics in the turbulent core. In this context it is instructive to see the conditional profiles of  $\langle \theta \rangle_I$  and  $\langle G_i G_i \rangle_I$  (already shown for the SG-TNTI in Fig. 13) but now in relation to the VO-TNTI. These are shown in Fig. 15 for the three simulations. As expected after

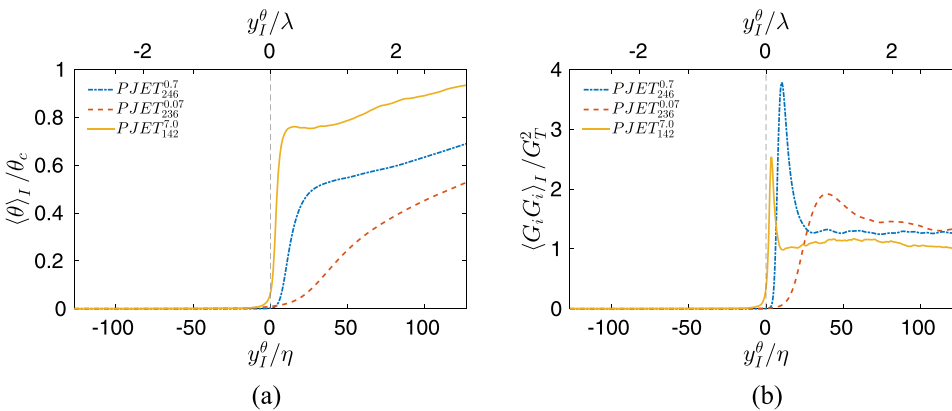


FIG. 13. Conditional profiles of (a) mean passive scalar concentration (normalised with the centreline concentration) and (b) mean magnitude of the passive scalar gradient (normalised with the centreline value) for the three DNS, (in relation to the SG-TNTI position). The upper axis with the Taylor scale normalisation corresponds to  $PJET_{246}^{0.7}$  only.

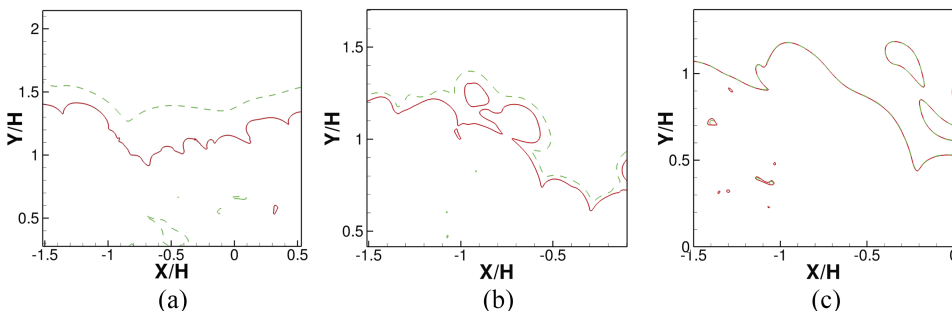


FIG. 14. Lines defining the detected velocity/vorticity TNTI (VO-TNTI) (red/solid line) and the scalar/scalar gradient TNTI (SG-TNTI) (green/dashed line) in a small section of the  $(x, y)$  plane for the three DNS used in the present work. (a)  $PJET_{236}^{0.07}$ , (b)  $PJET_{246}^{0.7}$  and (c)  $PJET_{142}^{7.0}$ .

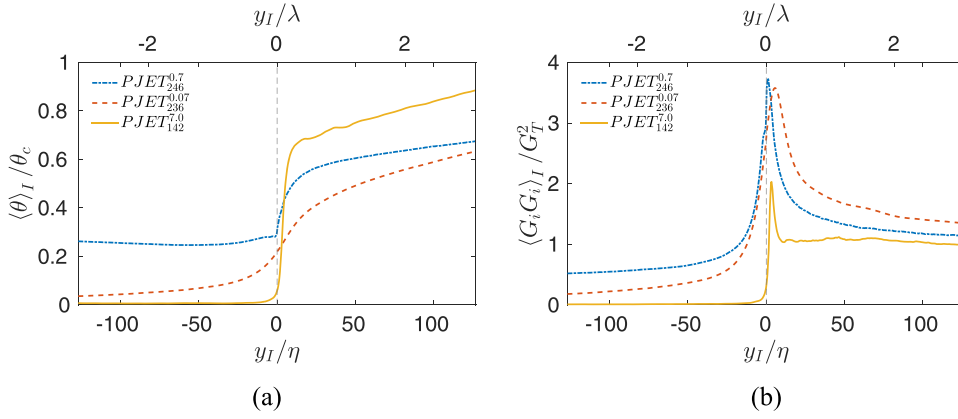


FIG. 15. Conditional profiles of (a) mean passive scalar concentration (normalised with the centreline concentration) and (b) mean magnitude of the passive scalar gradient (normalised with the centreline value) for the three DNS (in relation to the SG-TNTI position). The upper axis with the Taylor scale normalisation corresponds to  $PJET_{246}^{0.7}$  only.

comparing Figs. 2 and 3, Fig. 15(a) shows that there are substantial amounts of scalar outside the turbulent core region for  $PJET_{246}^{0.7}$  and  $PJET_{236}^{0.07}$ . As remarked by an anonymous referee, the higher values of passive scalar observed near the VO-TNTI in  $PJET_{246}^{0.7}$  reflects the smaller distance between the VO-TNTI and SG-TNTI observed for this case compared with  $PJET_{236}^{0.07}$ .

As in Fig. 13(b), the scalar gradient [Fig. 15(b)] exhibits a very marked peak in the VO-TNTI frame at roughly the same location, in agreement with Watanabe *et al.*<sup>19</sup> and Hunger *et al.*,<sup>20</sup> and in contrast with the conditional profiles in relation to the SG-TNTI [Fig. 13(b)], where the peaks occur at different locations. As expected, for  $PJET_{142}^{7.0}$  the scalar gradient is similar to before (compare  $PJET_{142}^{7.0}$  in Figs. 13 and 15—the smaller magnitude of the peak of  $\langle G_i G_i \rangle_I$  is due to the SG-TNTI and VO-TNTI not being exactly at the same location everywhere). The effect of the Schmidt number for the other cases can be observed in the “width” of the peak of  $\langle G_i G_i \rangle_I$ , which is wider for the lower Schmidt number case. As remarked by an anonymous referee, the simple fact that the SG-TNTI and VO-TNTI do not coincide will lead to differences in the dynamics of the scalar gradient for the three cases. This will be discussed in Sec. IV.

#### IV. THE PASSIVE SCALAR GRADIENT NEAR THE TURBULENT/NON-TURBULENT INTERFACE

In this section the scalar/scalar gradient turbulent/non-turbulent interface (SG-TNTI) will be analysed in detail. We start by studying the scalar gradient budgets for the three Schmidt numbers to discuss the scalar mixing dynamics, before addressing the detailed structure of the several layers existing inside the SG-TNTI for each Schmidt number. In the end the complete picture of the effects of the Schmidt number on the passive scalar mixing near a turbulent/non-turbulent interface emerges.

##### A. Conditional scalar gradient budgets at the turbulent/non-turbulent interface

In this section we analyse the scalar gradient budgets near the TNTI. The starting point is the scalar gradient transport equation written in the reference frame of the scalar gradient iso-surface detected as described before (Sec. III B). Applying the same methodology described in Sec. III A to the magnitude

of the scalar gradient  $G^2 = G_i G_i$ , we arrive at the passive scalar gradient transport equation written in a moving SG-TNTI,

$$\underbrace{\frac{\partial G^2/2}{\partial t}}_{\text{Temp. Variation}} = - \underbrace{(\mathbf{U}(x_I + x_0) - \mathbf{U}(x_0) - \mathbf{V}_P^G)}_{\text{Convection}} \cdot (\nabla G^2/2) + \underbrace{G_i G_j S_{ij}}_{\text{Production}} + \underbrace{\gamma \nabla^2 (G^2/2)}_{\text{Diffusion}} - \underbrace{\gamma (\nabla G)^2}_{\text{Dissipation}}. \quad (9)$$

The several terms represent the temporal variation of scalar gradient magnitude  $G^2/2$  due to convection, production, molecular diffusion, and molecular dissipation, respectively.  $\mathbf{V}_P^G$  is the propagation velocity of the passive scalar gradient interface, which can be computed by

$$\mathbf{V}_P^G = - \left( \frac{2G_i G_j S_{ij}}{|\nabla G^2|} + \frac{2\gamma \nabla^2 (G^2/2)}{|\nabla G^2|} - \frac{2\gamma (\nabla G)^2}{|\nabla G^2|} \right) \frac{\nabla G^2}{|\nabla G^2|}, \quad (10)$$

where again the first and second and third terms in the right-hand side of Eq. (10) represent the inviscid and viscous contributions to  $\mathbf{V}_P^G$ , respectively.

##### 1. SG-TNTI for $Sc = 0.7$

We start the analysis of the scalar gradient budgets with Fig. 16 showing the conditional scalar gradient budget [Eq. (9)] for the simulation  $PJET_{246}^{0.7}$ , where the several vertical lines represent the start of the SG-TNTI position ( $y_I^0/\eta = 0$ ), the IB, the end of the VSL, and end of the TSL (start of the turbulent core region), respectively. In order to facilitate the comparison between the several different Schmidt number cases, all the profiles have been normalised by the magnitude of the scalar gradient inside the turbulent core region at  $y_I/\eta = 300$ . At the turbulent core region,  $G^2$  is commanded by an approximate balance between production and molecular dissipation [Fig. 16(a)], as most of the other terms are only important near the SG-TNTI, in a small distance of  $0 \lesssim y_I^0/\eta \lesssim 25$  from the SG-TNTI. Interestingly, the VO-TNTI is completely outside this region in  $25 \lesssim y_I^0/\eta \lesssim 35$ , and despite its complexity (described before in Fig. 10) its effects do not seem to be noticed in any of the terms governing  $G^2$ . Indeed these terms are approximately constant from  $y_I^0/\eta \gtrsim 25$ .

It is interesting to observe how the build up of  $G^2$  is operated near the SG-TNTI [Fig. 16(b)]. The molecular diffusion

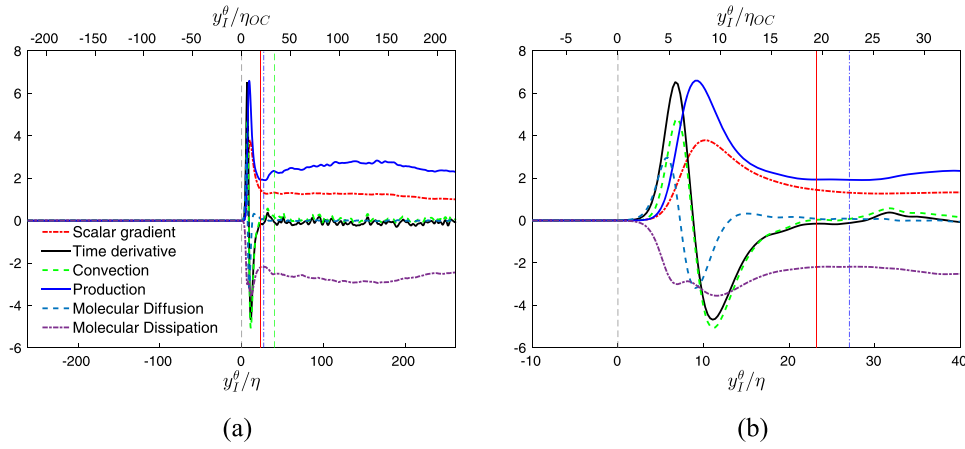


FIG. 16. Conditional budgets of passive scalar gradient  $G^2/2$  represented by the terms from Eq. (9) at the far field self-similar region of the temporal plane jet simulation  $PJET_{246}^{0.7}$  as a function of the distance from the SG-TNTI, normalised by the Kolmogorov micro-scale  $\eta$  and the Obukhov-Corrsin micro-scale  $\eta_{OC}$  from (a)  $-250 \leq y_1^{\theta}/\eta \leq +250$ , and (b)  $-10 \leq y_1^{\theta}/\eta \leq +40$ . All the curves have been normalised by the magnitude of the scalar gradient inside the turbulent core region at  $y_1/\eta = 300$ . The dashed vertical grey line is the start of the SG-TNTI position ( $y_1^{\theta}/\eta = 0$ ), detected with the magnitude of the scalar gradient (described in Sec. III B), while the vertical solid/red, dash-dot/blue and long-dash/green lines represent the IB, end of the VSL and end of the TSL (start of the turbulent core), respectively, associated with the velocity/vorticity TNTI.

starts the process, which is shortly after taken by the convection, rising into higher (term) values, and shortly afterwards by the production, which attains the highest peaks from all the terms governing the scalar mixing. The peak of  $G^2$  is right after the peak production. Notice that since this takes place in the irrotational region, the velocity associated with this convection term, as the strain associated with this production, is caused by the irrotational entrainment wind and irrotational velocity fluctuations near the interface,<sup>31</sup> respectively. Indeed “true turbulent mixing” is not possible at these locations, since the velocity and strain due to the turbulence are far behind this region. To the author’s knowledge, the only other existing reference where similar budgets have been analysed is in the work of Hunger *et al.*<sup>20</sup> In that work the budget of the scalar dissipation  $\varepsilon_{\theta}$  is analysed in relation to the VO-TNTI, whereas in the present work we analyse the scalar gradient magnitude ( $G_i G_i = \varepsilon_{\theta}/\gamma$ ) but in relation to the SG-TNTI. Another difference consists in the fact that in the present work the budgets are assessed taking into account the motion of the moving SG-TNTI (as described above), whereas this is not done in Hunger *et al.*<sup>20</sup> Nevertheless, the present results do show several similarities with the previous work: the importance of

the molecular diffusivity near the interface is observed in both works, as is the lack of balance between production and dissipation (of scalar gradient) at the same location, in contrast to what happens inside the turbulent core region.

The terms of molecular diffusion, convection, and production are closely linked to the build up of  $G^2$ . This can be appreciated by looking into the joint probability density functions (JPDFs) of the temporal variation of  $G^2$  and some of the terms at different locations near the SG-TNTI (the PDFs have been centred and normalised with their root-mean-square values). Figure 17 shows in particular the JPDFs of temporal variation and molecular diffusion at the molecular diffusion peak ( $y_1^{\theta}/\eta \approx 5.6$ ), and at the maximum convection ( $y_1^{\theta}/\eta \approx 7$ ), while Fig. 18 shows the JPDFs of temporal variation and production at the same locations. The molecular diffusion is clearly correlated with the temporal variation, increasing  $G^2$  for positive events of  $G^2$  diffusion (notice that the PDFs are centred and normalised so that the mean values are taken from the budgets at a given location). Negative events of diffusion appear to be depleted. A similar observation can be made for the production of  $G^2$ . The same JPDFs computed in other locations such as the IB or the turbulent core region

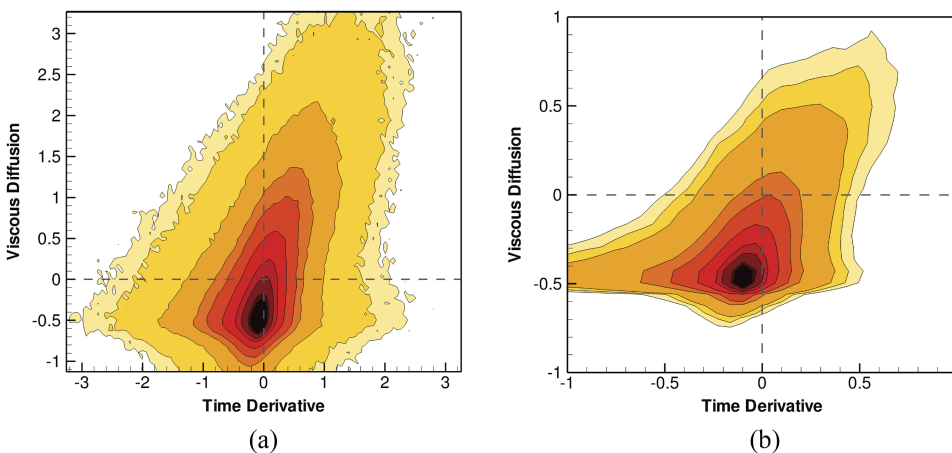


FIG. 17. Joint probability density functions (JPDFs) of temporal variation and molecular diffusion of  $G^2$  for  $PJET_{246}^{0.7}$  at (a) the molecular diffusion peak ( $y_1^{\theta}/\eta \approx 5.6$ ) and at the maximum convection ( $y_1^{\theta}/\eta \approx 7$ ). Dark/light (red/yellow) colours represent regions of high/low probability, respectively (the PDFs have been centred and normalised with their root-mean-square values).

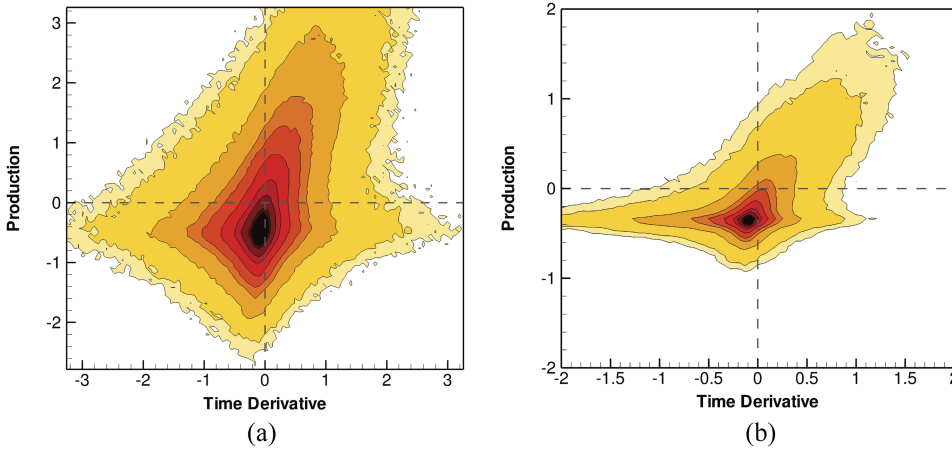


FIG. 18. Joint probability density functions (JPDFs) of temporal variation and production of  $G^2$  for  $PJET_{246}^{0.7}$  at (a) the molecular diffusion peak ( $y_1^\theta/\eta \approx 5.6$ ) and at the maximum convection ( $y_1^\theta/\eta \approx 7$ ). Dark/light (red/yellow) colours represent regions of high/low probability, respectively (the PDFs have been centred and normalised with their root-mean-square values).

exhibit no correlation at all and display similar (symmetric) positive/negative diffusion and production events (not shown). It is also interesting to remark how, as one moves from the first ( $y_1^\theta/\eta \approx 5.6$ ) to the second ( $y_1^\theta/\eta \approx 7$ ) of these locations, there is a slight decrease of the correlation level associated with the molecular diffusion and the production, thus confirming the changing relevance of the terms as one moves into different locations within the SG-TNTI.

## 2. SG-TNTI for $Sc = 0.07$

Figure 19 shows the conditional budget of  $G^2/2$  for  $PJET_{236}^{0.07}$ . This case differs from the previous one only on the Schmidt number since the turbulence features of the two flows, for the velocity/vorticity fields, are very similar. As in the previous case for  $Sc = 0.7$ , at the turbulent core region there is an approximate balance between production and molecular dissipation [Fig. 19(a)] and again most of the scalar mixing dynamics occurs completely outside the VO-TNTI. Whereas the scalar mixing takes place at  $0 \lesssim y_1^\theta/\eta \lesssim 60$ , the VO-TNTI layer is at  $62 \lesssim y_1^\theta/\eta \lesssim 75$ .

In contrast with  $Sc = 0.7$ , for  $Sc = 0.07$  the convective term is negligible throughout the SG-TNTI and the build up of  $G^2$  is

mainly operated first by the molecular diffusion and latter on by the production, with the maximum of  $G^2$  taking place after the production maximum. Thus the main difference between the  $Sc = 0.7$  and  $Sc = 0.07$  is the absence of an important role played by the convective term for  $Sc = 0.07$ , which is consistent with a bigger distance between the SG-TNTI and VO-TNTI in this case. Moreover, as in  $Sc = 0.7$  the strain responsible by the production term is solely due to the irrotational shear induced by the turbulent eddies in the turbulent core region close to the VO-TNTI. It is noteworthy that for the two cases with  $Sc < 1$  ( $PJET_{236}^{0.07}$  and  $PJET_{246}^{0.7}$ ) the first term dominating the transfer of  $G^2$  into the NT region is the molecular diffusion. This is consistent with the observation that the distance between the VO-TNTI and SG-TNTI is larger for the smaller  $Sc$  numbers. Similar different locations for the VO-TNTI and SG-TNTI are also observed when no noise is used to perturb the velocity and scalar fields at the start of the simulations.

Figure 20 shows the JPDFs of temporal variation and molecular diffusion, at the peak of molecular diffusion ( $y_1^\theta/\eta \approx 19$ ), and at the peak of  $G^2$  ( $y_1^\theta/\eta \approx 40$ ), again showing that at these locations  $G^2$  increases by molecular diffusion (which is also known from the budget), and how the events of negative

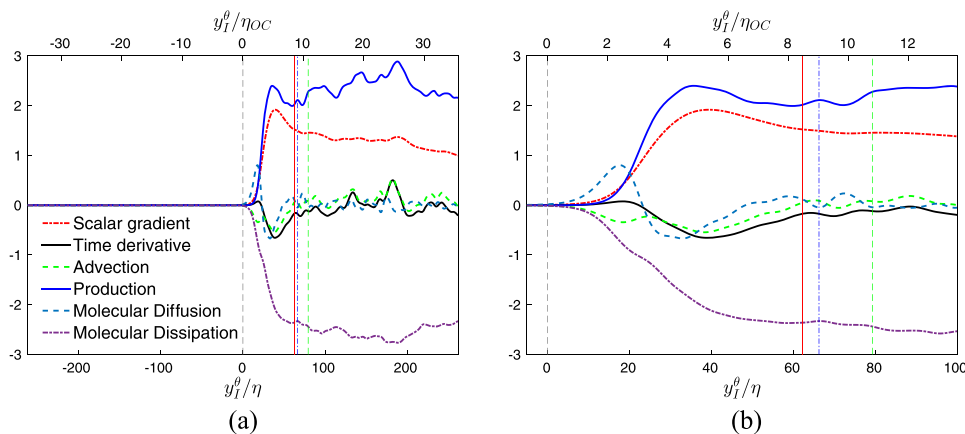


FIG. 19. Conditional budgets of passive scalar gradient  $G^2/2$  represented by the terms from Eq. (9) at the far field self-similar region of the temporal plane jet simulation  $PJET_{236}^{0.07}$  as a function of the distance from the SG-TNTI, normalised by the Kolmogorov micro-scale  $\eta$  and the Obukhov-Corrsin micro-scale  $\eta_{OC}$  from (a)  $-250 \leq y_1^\theta/\eta \leq +250$  and (b)  $-5 \leq y_1^\theta/\eta \leq +100$ . All the curves have been normalised by the magnitude of the scalar gradient inside the turbulent core region at  $y_1/\eta = 300$ . The dashed vertical grey line is the start of the SG-TNTI position ( $y_1^\theta/\eta = 0$ ), detected with the magnitude of the scalar gradient (described in Sec. III B), while the vertical solid/red, dash-dot/blue and long-dash/green lines represent the IB, end of the VSL and end of the TSL (start of the turbulent core), respectively, associated with the velocity/vorticity TNTI.

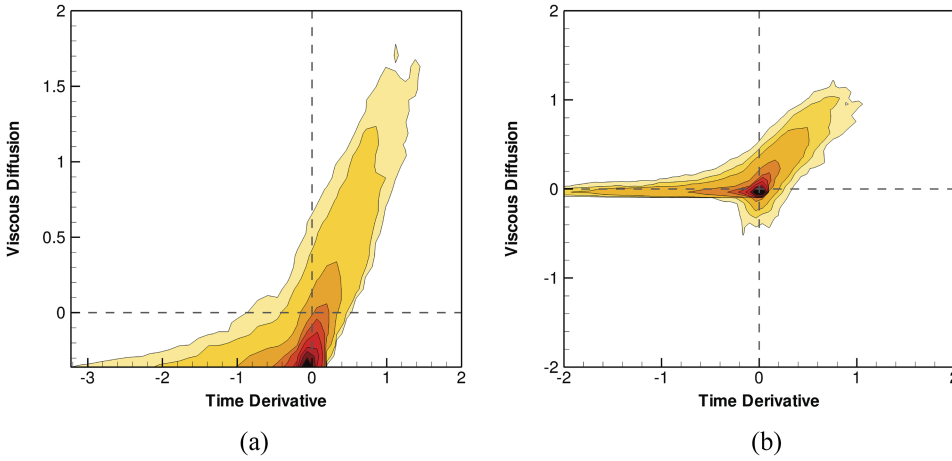


FIG. 20. Joint probability density functions (JPDFs) of temporal variation and molecular diffusion of  $G^2$  for  $PJET_{236}^{0.07}$  at (a) the molecular diffusion peak ( $y_1^\theta/\eta \approx 19$ ) and at the maximum of  $G^2$  ( $y_1^\theta/\eta \approx 40$ ). Dark/light (red/yellow) colours represent regions of high/low probability, respectively (the PDFs have been centred and normalised with their root-mean-square values).

diffusion are strongly suppressed. The same occurs in the JPDFs from the turbulent core region, where the JPDFs are symmetrical (not shown). The PDFs of production (not shown) exhibit similar trends.

### 3. SG-TNTI for $Sc = 7.0$

Finally, Fig. 21 shows the conditional budget of  $G^2/2$  for  $PJET_{142}^{7.0}$ . Again deep inside the turbulent region there is an approximate balance between production and dissipation of  $G^2$  [Fig. 21(a)]; however, we can see from the outset that the situation is very different to the previous cases, since now clearly the VO-TNTI and SG-TNTI overlap and turbulent fluctuations exist inside the SG-TNTI. Everything takes place in the small space between  $0 \lesssim y_1^\theta/\eta \lesssim 8$  because the turbulent fluctuations at the SG-TNTI strongly enhance the mixing. In contrast to the cases with  $Sc \leq 1$ , the molecular diffusion is now negligible throughout the SG-TNTI and the evolution of  $G^2$  at the SG-TNTI is solely commanded by the convective and production terms. The IB and start of the SG-TNTI almost coincide and allow to observe the interplay between the velocity and scalar fields in the very different flow physics of the VSL and TSL regions.

The production term seems to be dominating the mixing in the entire SG-TNTI, attaining its peak roughly at the boundary between the viscous superlayer (VSL) and the turbulent sublayer (TSL). Similar observation was reported by Watanabe *et al.*<sup>19</sup> The convective term on the other hand is observed to transport  $G^2$  from the TSL region into the VSL across this VSL/TSL boundary. Another (smaller) peak is observed in the convective term, very close to the IB/start of the SG-TNTI, suggesting that the double peak convection is caused by two different mechanisms in the SG-TNTI. One, more intense, probably linked to the fully non-linear nature of the velocity fluctuations as is found inside the TSL, and another, less strong, probably associated with the motion very close to the cores of the first row of eddies neighbouring the VO-TNTI.

Figure 22 shows the JPDFs of temporal variation and convection of  $G^2$  at the VSL/TSL boundary ( $y_1^\theta/\eta \approx 3$ ) and at the centre of the TSL ( $y_1^\theta/\eta \approx 10$ ). The correlation between the two quantities is very high; however, the figures also show that it tends to decrease very slightly, as one move into the interior of the turbulent region, reflecting the changing nature of the terms throughout the VO-TNTI and SG-TNTI layers.

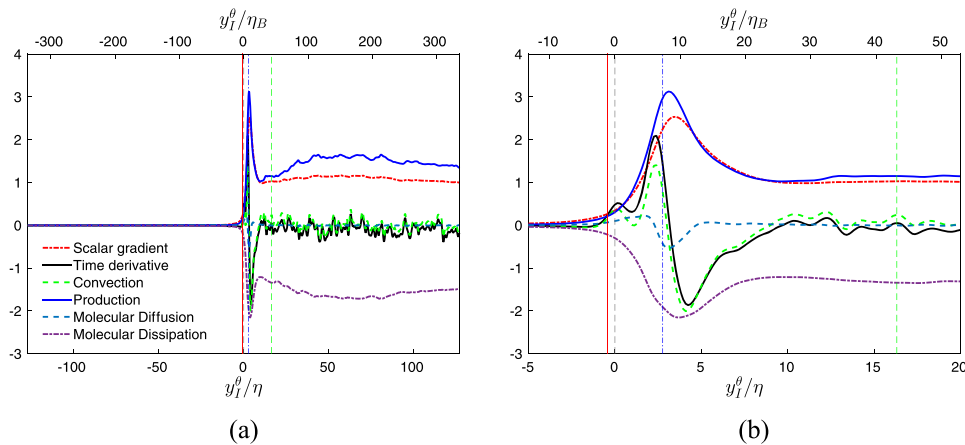


FIG. 21. Conditional budgets of passive scalar gradient  $G^2/2$  represented by the terms from Eq. (9) at the far field self-similar region of the temporal plane jet simulation  $PJET_{142}^{7.0}$ , as a function of the distance from the SG-TNTI, normalised by the Kolmogorov micro-scale  $\eta$  and the Batchelor micro-scale  $\eta_B$  from (a)  $-125 \leq y_1^\theta/\eta \leq +125$  and (b)  $-5 \leq y_1^\theta/\eta \leq +20$ . All the curves have been normalised by the magnitude of the scalar gradient inside the turbulent core region at  $y_1/\eta = 300$ . The dashed vertical grey line is the start of the SG-TNTI position ( $y_1^\theta/\eta = 0$ ), detected with the magnitude of the scalar gradient (described in Sec. III B), while the vertical solid/red, dash-dot/blue and long-dash/green lines represent the IB, end of the VSL, and end of the TSL (start of the turbulent core), respectively, associated with the velocity/vorticity TNTI.

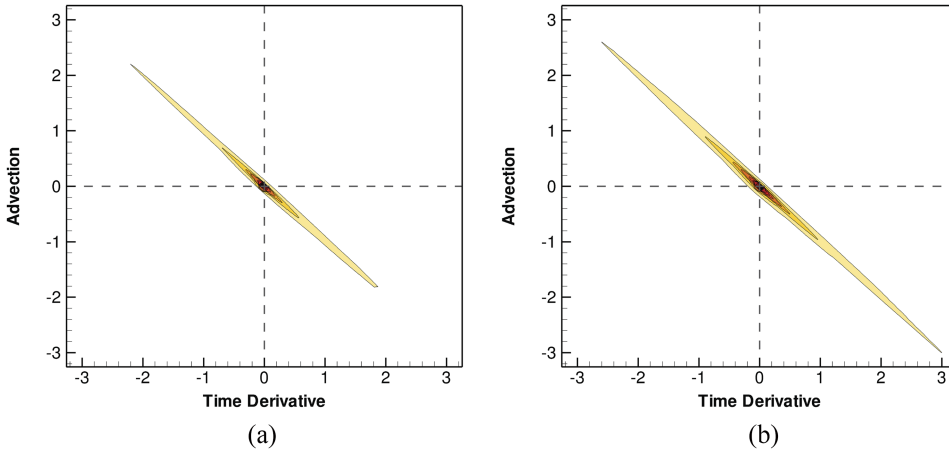


FIG. 22. Joint probability density functions (JPDFs) of temporal variation and convection of  $G^2$  for  $PJET_{142}^{7.0}$  at (a) the VSL/TSL boundary ( $y_1^\theta/\eta \approx 3$ ) and at the centre of the TSL ( $y_1^\theta/\eta \approx 10$ ). Dark/light (red/yellow) colours represent regions of high/low probability, respectively (the PDFs have been centred and normalised with their root-mean-square values).

## B. The structure of the scalar/scalar gradient turbulent/non-turbulent interface (SG-TNTI)

The results from Sec. IV A allow us to outline what the several sublayers existing within the scalar/scalar gradient turbulent/non-turbulent interface layer (SG-TNTI) are. Only two cases need to be considered,  $Sc \leq 1$  and  $Sc > 1$  because, as we have seen in Sec. IV A, the main difference regarding the cases  $Sc \approx 1$  ( $Sc = 0.7$ ) and  $Sc < 1$  ( $Sc = 0.07$ ) concerns the lack of importance of the convective term for  $Sc < 1$  ( $Sc = 0.07$ ).

The two cases are represented by sketches in Fig. 23. For  $Sc \leq 1$ , the SG-TNTI layer consists of (i) an external layer with irrotational velocity fluctuations, where the mixing occurs by molecular diffusion, and that we call the *irrotational-diffusive superlayer*, and (ii) a second (inner layer), where the mixing is mainly governed by the production, caused by the interaction of the scalar gradient and fluctuating irrotational strain. We call this second sublayer the *irrotational-straining sublayer*. When  $Sc > 1$ , the SG-TNTI presents an altogether different structure because there is no diffusive superlayer, as the entire SG-TNTI is now under the action of turbulent velocity fluctuations. For the highest Schmidt number studied in the present work ( $Sc = 7.0$ ), we have (i) an external sublayer where the mixing proceeds by the production of  $G^2$  controlled by “viscous” strain arising from the initial turbulent fluctuations within the viscous-superlayer and (ii) by a second sublayer where the production of  $G^2$  is governed by “inertial” strain existing in the turbulent sublayer (TSL). We call these two sub-layers the

*viscous-convective* and *inertial-convective* sublayers, respectively, and remark that they are very close, possibly coinciding, with the VSL and TSL regions, respectively, as in Watanabe *et al.*<sup>19</sup>

The local and mean thickness of these layers was computed from the present data. The irrotational-diffusive superlayer ( $Sc \leq 1$ ) can be defined as the distance from the start of the SG-TNTI until the point where the convective term takes over the growth of  $G^2$  (for  $Sc = 0.7$ ) or when the production term takes over that role (for  $Sc = 0.07$ ). We denote the thickness of this layer by  $\delta_\gamma^\theta$  to imply that molecular diffusivity  $\gamma$  is important in this region. In the present work we obtained mean values for these thicknesses equal to  $\langle \delta_\gamma^\theta \rangle / \eta = 7.4$  and  $\langle \delta_\gamma^\theta \rangle / \eta = 24.8$ , for  $Sc = 0.7$  and  $Sc = 0.07$ , respectively. The PDFs of the local thicknesses for this layer are indicated in Fig. 24(a) for  $Sc = 0.07$  and  $Sc = 0.7$ . The local thicknesses were simply computed by using the “local” conditional profiles of the scalar gradient budgets for each simulation. The PDFs display single well defined peaks that are near the mean values of its corresponding PDF; however,  $\delta_\gamma^\theta$  presents a wider range of possible values for  $Sc = 0.07$  than for  $Sc = 0.7$ . The thickness of the second sublayer  $\delta_S^\theta$  is defined by the distance between the end of the previous layer and the point where  $G^2$  attains its “turbulent core” value. Here the subscript  $S$  represents the strain rate effects governing the production.

For  $Sc > 1$ , we define the thickness of the viscous-convective superlayer  $\delta_V^\theta$  as the distance from the start of the SG-TNTI and the point of maximum production, while the

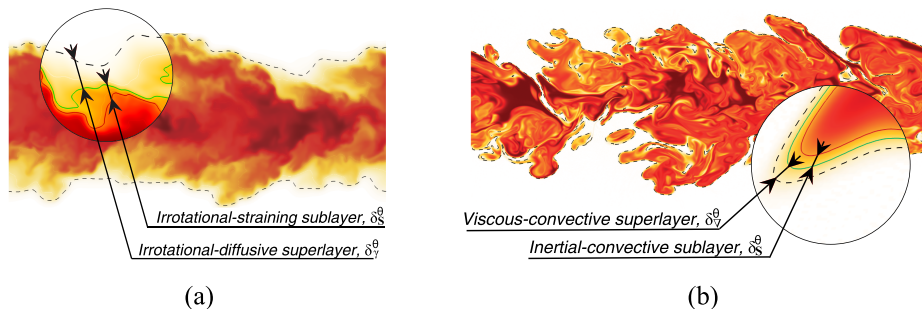


FIG. 23. Sketch representing the scalar/scalar gradient turbulent/non-turbulent interface layer (SG-TNTI) at the edge of the VO-TNTI, where darker/lighter colours represent more/less intense values of scalar concentration. The thicknesses of the irrotational-diffusive superlayer ( $\delta_\gamma^\theta$ ), viscous-convective superlayer ( $\delta_V^\theta$ ), irrotational-straining sublayer, and inertial-convective superlayer ( $\delta_S^\theta$ ) are also represented. (a)  $Sc \leq 1$  and (b)  $Sc > 1$ .

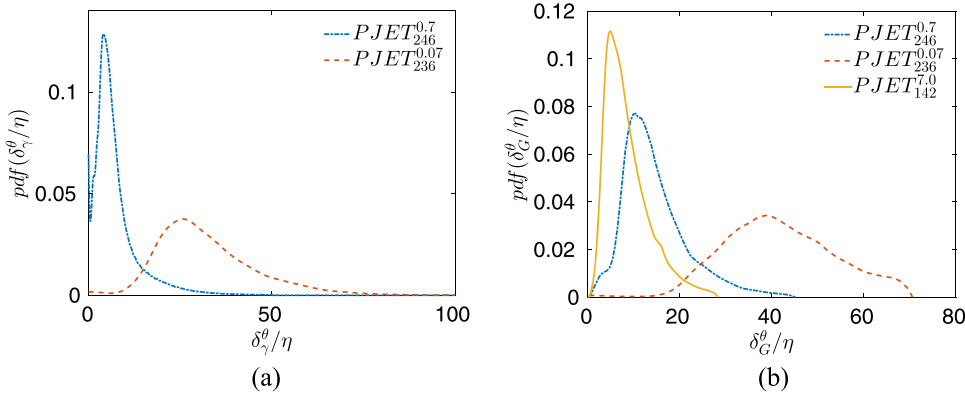


FIG. 24. Probability density functions of the irrotational-diffusive sublayers and of the SG-TNTI layer. (a) Local irrotational-diffusive sublayer thickness and (b) local SG-TNTI thickness.

thickness of the inertial-convective sublayer  $\delta_S^\theta$  is defined as the distance between this point and the location of the asymptotic turbulent value of  $G^2$ .

The total extent of the scalar-scalar gradient turbulent/non-turbulent interface (SG-TNTI), here denoted by  $\delta_G^\theta$ , is the counterpart of the thickness of the VO-TNTI  $\delta_\omega$ , defined in Ref. 2 and can be obtained by adding (for each case) the two sublayers. Thus we have

$$\begin{cases} \delta_G^\theta = \delta_\gamma^\theta + \delta_S^\theta, & \text{for } Sc \leq 1 \\ \delta_G^\theta = \delta_\gamma^\theta + \delta_S^\theta, & \text{for } Sc > 1 \end{cases}.$$

In the present work the mean value of the entire SG-TNTI was computed for the three DNS, giving  $\langle \delta_G^\theta \rangle / \eta = 8.7$ ,  $\langle \delta_G^\theta \rangle / \eta = 14.6$ , and  $\langle \delta_G^\theta \rangle / \eta = 41.0$  for  $Sc = 7$ ,  $Sc = 0.7$ , and  $Sc = 0.07$ , respectively. The PDFs of the local  $\delta_G^\theta$  are given in Fig. 24(b) and again show that the PDFs display peaks very near the mean values of  $\delta_G^\theta$ . It is noteworthy that for  $Sc = 0.07$  there seems to be a minimum possible value for  $\delta_G^\theta$ , below which no single values of  $\delta_G^\theta$  are found. The same occurs for this simulation regarding  $\delta_\gamma^\theta$ , and it is likely that the two facts are related since (for  $Sc \leq 1$ )  $\langle \delta_G^\theta \rangle = \langle \delta_\gamma^\theta \rangle + \langle \delta_S^\theta \rangle$ . Table II summarises the values of the mean thicknesses for the SG-TNTI and its sublayers for the three DNS used in the present work.

### C. The scaling of the scalar/scalar gradient turbulent/non-turbulent interface (SG-TNTI)

It would be interesting to establish and assess the scaling of each one of the layers described above, similarly as has been done for the VO-TNTI.<sup>2</sup> However, to carefully assess the scaling laws one needs a wide range of  $Re_\lambda$  and  $Sc$  numbers (at

sufficiently high  $Re_\lambda$ ), which we do not have at present. Moreover the resolution needed to directly measure the viscous-convective superlayer needs to be increased (which is why  $\delta_\nabla^\theta$  is absent from Table II). However, the present limitations do not prevent us from at least proposing several scaling laws for some of the layers, which could be assessed in future studies.

For  $Sc \leq 1$ , one should be careful while assessing these scaling laws because the characteristic scales of turbulence in the irrotational region are different from those inside the turbulent region. In particular, for distances from the VO-TNTI bigger than the integral scale of turbulence ( $|y_I|/L_{11} \gg 1$ ), for  $y_I$  in the NT region ( $y_I < 0$ ) Phillips<sup>53</sup> derived the following scaling laws:

$$\begin{cases} \langle u_{NT}^2 \rangle_I \sim |y_I|^{-4} \\ \langle \lambda_{NT}^2 \rangle_I \sim |y_I|^{+2} \\ \langle Re_\lambda^{NT} \rangle_I \sim |y_I|^{-1} \end{cases},$$

where  $\langle u_{NT}^2 \rangle_I$ ,  $\langle \lambda_{NT}^2 \rangle_I$ , and  $\langle Re_\lambda^{NT} \rangle_I$  are the velocity variance, Taylor micro-scale, and Taylor-based Reynolds number, respectively, in the irrotational (or non-turbulent) region at a distance from the IB  $y_I$ , larger than the integral scale  $L_{11}$  (and  $y_I < 0$ ).

For  $Sc \leq 1$ , one considers that at the irrotational-diffusive sublayer, the scalar gradient transport equation can be approximated by

$$\frac{DG^2}{Dt} \sim u_j \frac{\partial G^2}{\partial x_j} \sim \gamma \frac{\partial^2 G^2}{\partial x_j \partial x_j}, \quad (11)$$

so that the magnitude of the terms in the equation above can be approximated by the relation,

TABLE II. Mean thicknesses of the SG-TNTI and of their sublayers for the three turbulent planar jet DNS ( $PJET_{142}^{7.0}$ ,  $PJET_{236}^{0.07}$ , and  $PJET_{246}^{0.7}$ ), normalised by the Kolmogorov  $\eta$ , Obukhov-Corrsin  $\eta_{OC}$ , and Batchelor  $\eta_B$  micro-scales: Schmidt number,  $Sc$ ; Reynolds number based on the Taylor micro-scale at the self-similar regime,  $Re_\lambda$ ; SG-TNTI thickness  $\delta_G^\theta$ ; Irrotational-diffusive superlayer  $\delta_\gamma^\theta$  ( $Sc \leq 1$ ); Irrotational-straining sublayer  $\delta_S^\theta$  ( $Sc \leq 1$ ); Viscous-convective superlayer  $\delta_\nabla^\theta$  ( $Sc > 1$ ); Inertial-convective sublayer  $\delta_S^\theta$  ( $Sc > 1$ ).

	$Sc$	$Re_\lambda$	$\langle \delta_G^\theta \rangle / \eta$	$\langle \delta_G^\theta \rangle / \eta_{OC}$	$\langle \delta_G^\theta \rangle / \eta_B$	$\langle \delta_\gamma^\theta \rangle / \eta$	$\langle \delta_\gamma^\theta \rangle / \eta_{OC}$	$\langle \delta_S^\theta \rangle / \eta$	$\langle \delta_S^\theta \rangle / \eta_{OC}$	$\langle \delta_S^\theta \rangle / \eta_B$
$PJET_{142}^{7.0}$	7.0	141.9	8.7	...	23.5	...	...	(4–5)	...	(10.8–13.5)
$PJET_{236}^{0.07}$	0.07	236.3	41.0	5.5	...	24.8	3.4	16.2	2.2	...
$PJET_{246}^{0.7}$	0.7	246.2	14.6	11.2	...	7.4	5.7	7.2	5.5	...

$$\frac{\langle u_{NT}^2 \rangle_I^{1/2} \langle G^2 \rangle_I}{\langle \delta_\gamma^\theta \rangle} \sim \frac{\gamma \langle G^2 \rangle_I}{\langle \delta_\gamma^\theta \rangle^2}, \quad (12)$$

thus,

$$\frac{\langle u_{NT}^2 \rangle_I^{1/2}}{\langle \delta_\gamma^\theta \rangle} \sim \frac{\gamma}{\langle \delta_\gamma^\theta \rangle^2}, \quad (13)$$

and the mean thickness of the irrotational-diffusive sublayer is

$$\langle \delta_\gamma^\theta \rangle \sim \frac{\gamma}{\langle u_{NT}^2 \rangle_I^{1/2}}. \quad (14)$$

The above estimate is equivalent to assume that the thickness of the irrotational-diffusive superlayer is only governed by the scalar diffusivity, and by the velocity fluctuations in the irrotational region  $\delta_\gamma^\theta = \delta_\gamma^\theta(\gamma, u')$ ; therefore, the only dimensional possibility is  $\delta_\gamma^\theta \sim \gamma/u'$ , which leads to Eq. (14). From this equation we can write the scaling law for the mean thickness of the irrotational-diffusive superlayer,

$$\frac{\langle \delta_\gamma^\theta \rangle}{\eta} \sim S_c^{-1} \langle Re_\lambda^{NT} \rangle_I^{-1/2}. \quad (15)$$

The mean thickness of the viscous-convective superlayer  $\delta_\nabla^\theta$  can be estimated using our premise that the viscous-convective superlayer coincides with the viscous superlayer (VSL),

$$\langle \delta_\nabla^\theta \rangle \approx \langle \delta_\nu \rangle \sim \eta. \quad (16)$$

Furthermore, Taveira and da Silva<sup>12</sup> showed that the mean thickness of the VSL is  $\langle \delta_\nu \rangle / \eta \approx 4-5$ , and this value was used to estimate  $\langle \delta_\nabla^\theta \rangle$  in Table II. Using the values of the SG-TNTI thickness  $\delta_G^\theta$  and  $\delta_\gamma^\theta$  (for  $S_c \leq 1$ ) or  $\delta_\nabla^\theta$  (for  $S_c > 1$ ), the mean thicknesses of the irrotational-straining sublayer  $\delta_S^\theta$  and of the inertial-convective sublayer  $\delta_S^\theta$  can also be estimated (see Table II).

Finally, the mean thickness of the irrotational-straining superlayer  $\delta_S^\theta$  ( $S_c \leq 1$ ) and of the inertial-convective sublayer  $\delta_S^\theta$  ( $S_c > 1$ ) can be estimated assuming that in these layers the variation of  $G^2$  is dominated by the scalar gradient production,

$$\frac{DG^2}{Dt} \sim u_j \frac{\partial G^2}{\partial x_j} \sim G_i G_j S_{ij}, \quad (17)$$

where the magnitude of each term can be estimated as follows:

$$\frac{\langle u^2 \rangle_I^{1/2} \langle G^2 \rangle_I}{\langle \delta_S^\theta \rangle} \sim \langle G^2 \rangle_I \langle S \rangle_I, \quad (18)$$

and thus,

$$\langle \delta_S^\theta \rangle \sim \frac{\langle u^2 \rangle_I^{1/2}}{\langle S \rangle_I}, \quad (19)$$

where  $\langle S \rangle_I$  is the magnitude of the rate-of-strain tensor in the irrotational region (for  $S_c \leq 1$ ) or in the turbulent region (for  $S_c > 1$ ).

Therefore, in the irrotational-straining sublayer ( $S_c \leq 1$ ) we have

$$\langle \delta_S^\theta \rangle \sim \frac{\langle u_{NT}^2 \rangle_I^{1/2}}{\langle S_{NT} \rangle_I} \sim \langle \lambda_{NT} \rangle_I, \quad (20)$$

whereas in the inertial-convective sublayer ( $S_c > 1$ ) we have

$$\langle \delta_S^\theta \rangle \sim \frac{\langle u^2 \rangle_I^{1/2}}{\langle S \rangle_I} \sim \langle \lambda \rangle_I. \quad (21)$$

The above scaling laws should be addressed in future studies for a range of Schmidt numbers and at sufficiently large Reynolds numbers.

## V. CONCLUSIONS

Three direct numerical simulations (DNS) of turbulent planar jets with Reynolds numbers ranging from  $142 \leq Re_\lambda \leq 246$  and Schmidt numbers from  $0.07 \leq S_c \leq 7.0$  were used to analyse the dynamics of the passive scalar gradient near a turbulent/non-turbulent interface (TNTI). The TNTI is analysed in all the flows in the far field fully developed region where the probability density functions of the passive scalar across the jet are of ‘‘marching-type’’ form.

For approximately the same Reynolds number, higher Schmidt numbers result on a steeper scalar gradient jump in the TNTI and a more corrugated passive scalar interface at the jet edge. A scalar-gradient turbulent/non-turbulent interface (SG-TNTI) is observed in the three simulations that does not coincide with the vorticity turbulent/non-turbulent interface (VO-TNTI) defined in previous studies, distancing between 10 and 30 Kolmogorov micro-scale. The outer boundary of the SG-TNTI is detected in a similar way as the VO-TNTI<sup>9</sup> using a scalar-gradient threshold based on ‘‘turbulent scalar’’ volume within the jet shear layer. The distance between the outer boundary of the SG-TNTI and the VO-TNTI, the so-called irrotational boundary<sup>18</sup> is larger for  $S_c = 0.07$  than for  $S_c = 0.7$ , while the two outer boundaries coincide for  $S_c = 7.0$ .

Conditional scalar gradient budgets show that for  $S_c = 0.07$  and  $0.7$  a *diffusive superlayer* emerges at the SG-TNTI, where the scalar gradient diffusion dominates, while the production is negligible, the main difference between the SG-TNTI layers being that for  $S_c = 0.07$  the scalar gradient convection is negligible and the initial evolution of the scalar gradient proceeds almost entirely by molecular diffusion. For  $S_c = 0.07$  and  $0.7$ , this outer layer is followed by an *irrotational-straining sublayer* where the scalar gradient production dominates.

In contrast for  $S_c = 7.0$  the SG-TNTI consists of a *viscous-convective superlayer*, which closely matches the viscous superlayer from the VO-TNTI and by an *inertial-convective sublayer*, where scalar gradient production dominates and that is much smaller than the turbulent sublayer of the VO-TNTI.

The scaling laws and mean thicknesses of each one of these (sub)layers are briefly discussed. The careful assessment of the scaling laws pertaining to each one of these (sub)layers should be assessed in a future work.

## ACKNOWLEDGMENTS

This work has been supported by Fundaao para a Ciencia e a Tecnologia (FCT), through IDMEC, under LAETA, Project No. UID/EMS/50022/2013 and through Project No. PTDC/EMS-ENE/6129/2014.

The authors acknowledge the Laboratory for Advanced Computing at University of Coimbra for providing HPC,

computing and consulting resources that have contributed to the research results reported within this paper. URL <http://www.lca.uc.pt>

- <sup>1</sup>P. E. Dimotakis, "Turbulent mixing," *Annu. Rev. Fluid Mech.* **37**, 329–356 (2005).
- <sup>2</sup>C. B. da Silva, J. C. R. Hunt, I. Eames, and J. Westerweel, "Interfacial layers between regions of different turbulent intensity," *Annu. Rev. Fluid Mech.* **46**, 567–590 (2014).
- <sup>3</sup>A. A. Townsend, "The mechanism of entrainment in free turbulent flows," *J. Fluid Mech.* **26**, 689–715 (1966).
- <sup>4</sup>J. Mathew and A. Basu, "Some characteristics of entrainment at a cylindrical turbulent boundary," *Phys. Fluids* **14**(7), 2065–2072 (2002).
- <sup>5</sup>S. Corrsin and A. L. Kistler, "Free-stream boundaries of turbulent flows," Technical Report TN-1244, NACA, 1955.
- <sup>6</sup>J. Westerweel, C. Fukushima, J. M. Pedersen, and J. C. R. Hunt, "Mechanics of the turbulent-nonturbulent interface of a jet," *Phys. Rev. Lett.* **95**, 174501 (2005).
- <sup>7</sup>J. Westerweel, C. Fukushima, J. M. Pedersen, and J. C. R. Hunt, "Momentum and scalar transport at the turbulent/non-turbulent interface of a jet," *J. Fluid Mech.* **631**, 199–230 (2009).
- <sup>8</sup>M. Holzner, A. Liberzon, N. Nikitin, W. Kinzelbach, and A. Tsinober, "Small-scale aspects of flows in proximity of the turbulent/nonturbulent interface," *Phys. Fluids* **19**, 071702 (2007).
- <sup>9</sup>R. R. Taveira, J. S. Diogo, D. C. Lopes, and C. B. da Silva, "Lagrangian statistics across the turbulent-nonturbulent interface in a turbulent plane jet," *Phys. Rev. E* **88**, 043001 (2013).
- <sup>10</sup>R. R. Taveira and C. B. da Silva, "Kinetic energy budgets near the turbulent/nonturbulent interface in jets," *Phys. Fluids* **25**, 015114 (2013).
- <sup>11</sup>C. B. da Silva and R. R. Taveira, "The thickness of the turbulent/nonturbulent interface is equal to the radius of the large vorticity structures near the edge of the shear layer," *Phys. Fluids* **22**, 121702 (2010).
- <sup>12</sup>R. R. Taveira and C. B. da Silva, "Characteristics of the viscous superlayer in free shear turbulence and in planar turbulent jets," *Phys. Fluids* **26**, 021702 (2014).
- <sup>13</sup>T. Watanabe, C. B. da Silva, Y. Sakai, K. Nagata, and T. Hayase, "Lagrangian properties of the entrainment across turbulent/non-turbulent interface layers," *Phys. Fluids* **23**(8), 031701 (2016).
- <sup>14</sup>T. Watanabe, Y. Sakai, K. Nagata, Y. Ito, and T. Hayase, "Enstrophy and passive scalar transport near the turbulent/non-turbulent interface in a turbulent planar jet flow," *Phys. Fluids* **26**, 105103 (2014).
- <sup>15</sup>A. Attili, J. C. Cristancho, and F. Bisetti, "Statistics of the turbulent/non-turbulent interface in a spatially developing mixing layer," *J. Turbul.* **15**, 555–568 (2014).
- <sup>16</sup>M. Gampert, V. Narayanaswamy, P. Schaefer, and N. Peters, "Conditional statistics of the turbulent/non-turbulent interface in a jet flow," *J. Fluid Mech.* **731**, 615–638 (2013).
- <sup>17</sup>M. Gampert, K. Kleinheinz, N. Peters, and H. Pitsch, "Experimental and numerical study of the scalar turbulent/non-turbulent interface layer in a jet flow," *Flow, Turbul. Combust.* **92**, 429–449 (2013).
- <sup>18</sup>T. Watanabe, Y. Sakai, K. Nagata, Y. Ito, and T. Hayase, "Reactive scalar field near the turbulent/non-turbulent interface in a planar jet with a second-order chemical reaction," *Phys. Fluids* **26**, 105111 (2014).
- <sup>19</sup>T. Watanabe, Y. Sakai, K. Nagata, Y. Ito, and T. Hayase, "Turbulent mixing of passive scalar near turbulent and non-turbulent interface in mixing layers," *Phys. Fluids* **27**, 085109 (2015).
- <sup>20</sup>F. Hunger, M. Gauding, and C. Hasse, "On the impact of the turbulent/non-turbulent interface on differential diffusion in a turbulent jet flow," *J. Fluid Mech.* **802**, R5 (2016).
- <sup>21</sup>C. Pierce and P. Moin, "A dynamic model for subgrid-scale variance and dissipation rate of a conserved scalar," *Phys. Fluids* **10**(12), 3041–3044 (1998).
- <sup>22</sup>A. W. Cook and W. K. Bushe, "A subgrid-scale model for the scalar dissipation rate in nonpremixed combustion," *Phys. Fluids* **11**(3), 746–748 (1999).
- <sup>23</sup>B. Ganapathisubramani, K. Lakshminarasimhan, and N. T. Clemens, "Investigation of three-dimensional structure of fine scales in a turbulent jet by using cinematographic stereoscopic particle image velocimetry," *J. Fluid Mech.* **598**, 141–175 (2008).
- <sup>24</sup>J. Schumacher, K. Sreenivasan, and P. Young, "Very fine structures in scalar mixing," *J. Fluid Mech.* **531**, 113–122 (2005).
- <sup>25</sup>J. Schumacher and K. Sreenivasan, "Statistics and geometry of passive scalars in turbulence," *Phys. Fluids* **17**, 125107 (2005).
- <sup>26</sup>G. R. Ruetsch and M. R. Maxey, "Small-scale features of vorticity and passive scalar fields in homogeneous isotropic turbulence," *Phys. Fluids A* **3**, 1587, 1597 (1991).
- <sup>27</sup>G. R. Ruetsch and M. R. Maxey, "The evolution of small-scale structures in homogeneous isotropic turbulence," *Phys. Fluids A* **4**, 2747–2760 (1992).
- <sup>28</sup>M. Gampert, J. Boschung, F. Hennig, M. Gauding, and N. Peters, "The vorticity versus the scalar criterion for the detection of the turbulent/nonturbulent interface," *J. Fluid Mech.* **750**, 578–596 (2014).
- <sup>29</sup>C. Canuto, M. Y. Hussaini, A. Quarteroni, and T. A. Zang, *Spectral Methods in Fluid Dynamics* (Springer-Verlag, 1987).
- <sup>30</sup>J. H. Williamson, "Low-storage Runge-Kutta schemes," *J. Comput. Phys.* **35**, 48–56 (1980).
- <sup>31</sup>C. B. da Silva and J. C. F. Pereira, "Invariants of the velocity-gradient, rate-of-strain, and rate-of-rotation tensors across the turbulent/nonturbulent interface in jets," *Phys. Fluids* **20**, 055101 (2008).
- <sup>32</sup>C. B. da Silva, R. J. N. dos Reis, and J. C. F. Pereira, "The intense vorticity structures near the turbulent/non-turbulent interface a jet," *J. Fluid Mech.* **685**, 165–190 (2011).
- <sup>33</sup>S. Stanley and S. Sarkar, "Influence of nozzle conditions and discrete forcing on turbulent planar jets," *AIAA J.* **38**, 1615–1623 (2000).
- <sup>34</sup>S. Stanley, S. Sarkar, and J. P. Mellado, "A study of the flow-field evolution and mixing in a planar turbulent jet using direct numerical simulation," *J. Fluid Mech.* **450**, 377–407 (2002).
- <sup>35</sup>C. B. da Silva and O. Métais, "On the influence of coherent structures upon interscale interactions in turbulent plane jets," *J. Fluid Mech.* **473**, 103–145 (2002).
- <sup>36</sup>C. B. da Silva and J. C. F. Pereira, "The effect of subgrid-scale models on the vortices computed from large-eddy simulations," *Phys. Fluids* **16**, 4506–4534 (2004).
- <sup>37</sup>C. Le Ribault, S. Sarkar, and S. A. Stanley, "Large eddy simulation of evolution of a passive scalar in plane jet," *AIAA J.* **38**, 1509–1516 (2001).
- <sup>38</sup>E. Gutmark and I. Wygnansky, "The planar turbulent jet," *J. Fluid Mech.* **73**, 465–495 (1976).
- <sup>39</sup>R. Ramaprian and M. S. Chandrasekhara, "LDA measurements in plane turbulent jets," *J. Fluids Eng.* **107**, 264–271 (1985).
- <sup>40</sup>A. Davies, J. F. Keffer, and W. D. Baines, "Spread of a heated plane turbulent jet," *Phys. Fluids* **18**, 770–775 (1975).
- <sup>41</sup>P. E. Jenkins and V. W. Goldschmidt, "Mean temperature and velocity in a plane turbulent jet," *J. Fluids Eng.* **95**, 581–584 (1973).
- <sup>42</sup>M. van Reeuwijk and M. Holzner, "The turbulence boundary of a temporal jet," *J. Fluid Mech.* **739**, 254–275 (2014).
- <sup>43</sup>M. M. Rogers and R. D. Moser, "Direct simulation of a self-similar turbulent mixing layer," *Phys. Fluids* **6**(2), 903–923 (1994).
- <sup>44</sup>A. S. Monin and A. M. Yaglom, *Statistical Fluid Mechanics: Mechanics of Turbulence* (MIT Press, Cambridge, 1975), Vol. 2.
- <sup>45</sup>R. R. Prasad and K. R. Sreenivasan, "Scalar interfaces in digital images of turbulent flows," *Exp. Fluids* **7**(4), 259–264 (1989).
- <sup>46</sup>C. B. da Silva, R. R. Taveira, and G. Borrell, "Characteristics of the turbulent-nonturbulent interface in boundary layers, jets and shear-free turbulence," *J. Phys.: Conf. Ser.* **506**, 012015 (2014).
- <sup>47</sup>D. K. Bisset, J. C. R. Hunt, and M. M. Rogers, "The turbulent/non-turbulent interface bounding a far wake," *J. Fluid Mech.* **451**, 383–410 (2002).
- <sup>48</sup>C. B. da Silva and R. J. N. dos Reis, "The role of coherent vortices near the turbulent/non-turbulent interface in a planar jet," *Philos. Trans. R. Soc., A* **369**, 738–7531 (2011).
- <sup>49</sup>M. Holzner and B. Lüthi, "Laminar superlayer at the turbulence boundary," *Phys. Rev. Lett.* **106**, 134503 (2011).
- <sup>50</sup>K. Chauhan, J. Philip, and I. Marusic, "Scaling of the turbulent/non-turbulent interface in boundary layers," *J. Fluid Mech.* **751**, 298–328 (2014).
- <sup>51</sup>T. Watanabe, Y. Sakai, K. Nagata, Y. Ito, and T. Hayase, "Vortex stretching and compression near the turbulent/non-turbulent interface in a planar jet," *J. Fluid Mech.* **758**, 754–784 (2014).
- <sup>52</sup>M. Holzner, A. Liberzon, N. Nikitin, B. Lüthi, W. Kinzelbach, and A. Tsinober, "A Lagrangian investigation of the small-scale features of turbulent entrainment through particle tracking and direct numerical simulation," *J. Fluid Mech.* **598**, 465–475 (2008).
- <sup>53</sup>O. M. Phillips, "The irrotational motion outside a free turbulent boundary," *Math. Proc. Cambridge Philos. Soc.* **51**, 220 (1955).